Nanoscale dynamics of peptidoglycan assembly during the cell cycle of Streptococcus pneumoniae

Jennyfer Trouve, André Zapun, Christopher Arthaud, Claire Durmort, Anne Marie Di Guilmi, Bill Söderström, Anais Pelletier, Christophe Grangeasse, Dominique Bourgeois, Yung-Sing Wong, et al.

Article

Current Biology

Nanoscale dynamics of peptidoglycan assembly during the cell cycle of *Streptococcus pneumoniae*

Highlights

- Metabolic labeling allows dSTORM analysis of pneumococcal peptidoglycan synthesis
- Septal and peripheral peptidoglycan syntheses progress separately
- Septal peptidoglycan is synthesized and remodeled from the start of the cell cycle
- Peripheral synthesis persists after septal synthesis is completed

Authors

Jennyfer Trouve, André Zapun, Christopher Arthaud, ..., Dominique Bourgeois, Yung-Sing Wong, Cecile Morlot

Correspondence

cecile.morlot@ibs.fr

In brief

Synthesis of the cell wall ensures proper bacterial shape and integrity. Trouve et al. use a combination of cell labeling, single-molecule localization microscopy, and modeling to provide the first nanoscale description of cell wall assembly in *Streptococcus pneumoniae*, bringing new insights for bacterial morphogenesis.

Trouve et al., 2021, Current Biology *31*, 1–13
July 12, 2021
https://doi.org/10.1016/j.cub.2021.04.041

CellPress

Please cite this article in press as: Trouve et al., Nanoscale dynamics of peptidoglycan assembly during the cell cycle of *Streptococcus pneumoniae*, Current Biology (2021), https://doi.org/10.1016/j.cub.2021.04.041

Current Biology

CellPress
OPEN ACCESS

Article

Nanoscale dynamics of peptidoglycan assembly during the cell cycle of *Streptococcus pneumoniae*

Jennyfer Trouve,[1] André Zapun,[1] Christopher Arthaud,[1] Claire Durmort,[1] Anne Marie Di Guilmi,[1,6] Bill Söderström,[2,3] Anais Pelletier,[4] Christophe Grangeasse,[4] Dominique Bourgeois,[1] Yung-Sing Wong,[5] and Cecile Morlot[1,7,8,*]

[1]Univ. Grenoble Alpes, CNRS, CEA, IBS, 38000 Grenoble, France
[2]The ithree institute, University of Technology Sydney, Ultimo, NSW 2007, Australia
[3]Structural Cellular Biology Unit, Okinawa Institute of Science and Technology, 904-0495 Okinawa, Japan
[4]Molecular Microbiology and Structural Biochemistry (MMSB), CNRS, Univ. Lyon 1, UMR 5086, Lyon 69007, France
[5]Univ. Grenoble Alpes, CNRS, DPM, 38000 Grenoble, France
[6]Present address: Institute of Cellular and Molecular Radiobiology, Institut de Biologie François Jacob, CEA, Univ. Paris and Univ. Paris Sud, 92265 Fontenay aux Roses, France
[7]Twitter: @morlotcecile
[8]Lead contact
*Correspondence: cecile.morlot@ibs.fr
https://doi.org/10.1016/j.cub.2021.04.041

SUMMARY

Dynamics of cell elongation and septation are key determinants of bacterial morphogenesis. These processes are intimately linked to peptidoglycan synthesis performed by macromolecular complexes called the elongasome and the divisome. In rod-shaped bacteria, cell elongation and septation, which are dissociated in time and space, have been well described. By contrast, in ovoid-shaped bacteria, the dynamics and relationships between these processes remain poorly understood because they are concomitant and confined to a nanometer-scale annular region at midcell. Here, we set up a metabolic peptidoglycan labeling approach using click chemistry to image peptidoglycan synthesis by single-molecule localization microscopy in the ovoid bacterium *Streptococcus pneumoniae*. Our nanoscale-resolution data reveal spatiotemporal features of peptidoglycan assembly and fate along the cell cycle and provide geometrical parameters that we used to construct a morphogenesis model of the ovoid cell. These analyses show that septal and peripheral peptidoglycan syntheses first occur within a single annular region that later separates in two concentric regions and that elongation persists after septation is completed. In addition, our data reveal that freshly synthesized peptidoglycan is remodeled all along the cell cycle. Altogether, our work provides evidence that septal peptidoglycan is synthesized from the beginning of the cell cycle and is constantly remodeled through cleavage and insertion of material at its periphery. The ovoid-cell morphogenesis would thus rely on the relative dynamics between peptidoglycan synthesis and cleavage rather than on the existence of two distinct successive phases of peripheral and septal synthesis.

INTRODUCTION

Bacterial morphogenesis is intimately linked to synthesis of the peptidoglycan (PG), a giant cage-like polymer that confers cell shape and resistance to turgor pressure. PG consists of glycan chains cross-linked by peptide bridges.[1] Importantly for this study, synthesis of its cytosolic precursor (the lipid II), which is a N-acetylglucosamine-N-acetylmuramic acid disaccharide pentapeptide anchored to the plasma membrane, involves the addition of the last two residues of the peptide chain as a D-alanyl-D-alanine dipeptide (called DA-DA henceforth).[2] After flipping to the extracellular face of the membrane, the lipid II provides the building unit for the assembly of new PG, which results from the polymerization of glycan chains by transglycosylase (TG) activities and cross-linking of peptide chains by transpeptidase (TP) activities. TG activities are carried out by class A PBPs (penicillin-binding proteins) and SEDS proteins (shape, elongation, division, and sporulation) while TP activities are performed by class A and class B PBPs.[3,4] Cell morphogenesis not only involves PG synthesis but also PG modifications, such as limited cleavage by hydrolases, that will tune its shape and elasticity.[5] Genetic, cellular, and biochemical evidence suggests that synthetic and hydrolytic activities required to achieve a mature mesh of PG are coordinated within large protein complexes called the elongasome and the divisome.[6,7]

In rod-shaped bacteria, the elongasome is organized by the actin-like protein MreB and inserts PG on the cylindrical part of the cell before the divisome is recruited by the tubulin-like protein FtsZ at midcell for septal cross-wall synthesis.[8] The morphological group of ovococci, which includes *Streptococcus pneumoniae* and several other human pathogens (enterococci and streptococci), possess many proteins of the rods' elongasome but lack MreB.[9,10] In these bacteria, the annular structure formed by FtsZ (the Z-ring) at midcell drives the localization of elongation

Please cite this article in press as: Trouve et al., Nanoscale dynamics of peptidoglycan assembly during the cell cycle of *Streptococcus pneumoniae*, Current Biology (2021), https://doi.org/10.1016/j.cub.2021.04.041

and division proteins at the beginning of the cell cycle.[11–16] Throughout the cell cycle, all these proteins migrate toward the center of the division plane, but the class B PBP2x, a key player of the divisome, will progress faster and separate from other PG synthesis proteins.[17,18] This spatial uncoupling supports the idea that, although both localized at midcell, two different modes of PG synthesis occur for cell septation (septal PG synthesis) and elongation (peripheral PG synthesis) and more generally for morphogenesis of the ovoid cell. In agreement with this hypothesis, inactivation of divisome components leads to septation defects while inactivation of elongasome components leads to shorter cells.[17,19–21] Despite these fundamental observations, we still do not fully understand how PG is synthesized and modified to generate the ovoid shape. A major drawback in investigating this question is the fact that PG is assembled within an annular region whose dimensions approximate the resolution limit imposed by the diffraction of light.[17,18,22] To gain access to nanoscale details of PG assembly, we thus set up a bioorthogonal fluorescent labeling method—based on metabolic incorporation of a D-Ala analog and copper-free click chemistry[23]—followed by dSTORM (direct stochastic optical reconstruction microscopy).[24] In addition, we generated a dynamic geometrical model that allows analysis and interpretation of the experimental localization patterns. To shed light on dynamic features that are important for cell morphogenesis, experiments were performed on two widely studied pneumococcal strains, R800 and D39 *Δcps* (called D39$_{\Delta cps}$ henceforth), which lack part of the operon encoding the capsule. The relationships between key morphogenetic proteins, such as GpsB and DivIVA, vary between these two strains, which display significantly different phenotypes when those genes are mutated. GpsB was proposed to serve as a scaffold that concentrates morphogenetic proteins at PG synthesis sites and is required for proper septation of *S. pneumoniae*.[11,25,26] DivIVA interacts with several division proteins; it has a yet-to-be-understood function in PG synthesis and remodeling, including septum splitting and cell elongation in *S. pneumoniae*.[11,21,27] The *gpsB* gene is not essential in the R800 strain, and deletion of *divIVA* is epistatic to that of *gpsB*, while in D39, *gpsB* is essential in the presence or absence of *divIVA*.[11,25] Although not entirely understood, the differences between the two strains is linked to mutations in some cell cycle and cell wall genes like that encoding the class A PBP1a. Analysis of PG synthesis in R800 and D39$_{\Delta cps}$ by dSTORM lays the foundations for pneumococcal morphogenesis and highlights differences between these strains. Altogether, our work provides unprecedented data that uncover novel aspects of PG assembly and processing in *S. pneumoniae*, consistent with a morphogenesis mechanism based on synthesis of septal PG followed by cleavage coupled to insertion of peripheral PG in the freshly cleaved region.

RESULTS

Metabolic labeling of new PG in *S. pneumoniae* for dSTORM imaging

To label new PG through lipid II synthesis, using a probe that introduces minimal chemical modifications and can be extemporarily coupled to a dSTORM dye, we synthesized a DA-DA dipeptide carrying an N-terminal azide group (called aDA-DA henceforth; Figures S1A and S1B). Septal epifluorescence signal was clearly detected when *S. pneumoniae* R800 cells were pulse labeled for 5 min with 2.5 mM of aDA-DA, followed by incubation with Alexa Fluor 647 (AF647) fused to DIBO, which specifically and spontaneously reacts with azide groups (Figures 1A, S1C, and S2A). Cell shape was not affected (Figure S2B), and sacculi purification showed that aDA-DA is integrated into new PG (Figure S2C). In support of the idea that aDA-DA is incorporated through the lipid II synthesis pathway, as previously reported in *Escherichia coli*,[23] aDA-DA labeling was still observed when R800 cells were grown in the presence of D-cycloserine, which inhibits the D-Ala racemase and D-Ala-D-Ala ligase responsible for synthesis of the DA-DA dipeptide, as well as TP activities (Figure S2D).[28,29] By contrast, no labeling was observed when cells were incubated with the azido-D-Ala analog (aDA) in the presence of D-cycloserine (Figure S2D). These observations indicate that aDA-DA is intracellularly incorporated in place of the physiological DA-DA dipeptide into lipid II and is therefore a relevant probe to monitor PG synthesis, including the polymerization of glycan chains.

Labeling of R800 cells with a 5-min pulse using aDA-DA provided dSTORM images of high quality (Figure 1B), with a mean localization precision of about 12 nm and spatial resolution down to 30 nm. Decreasing the incubation time to increase the time resolution of our experiments decreased the signal-to-noise ratio and the resolution of the dSTORM images (Figure S2E). Using a 5-min incubation period, the localization of fluorophores at parental and daughter-cell division sites (called "equatorial" positions henceforth) was straightforward and the regions of PG synthesis could be analyzed with unprecedented resolution.

Analysis of pneumococcal cell morphology

On microscopy slides, pneumococcal cells lie along their longitudinal axis, and in this orientation, the labeled PG regions form bands resulting from the projection of annular labeling (Figure 2A). The dSTORM localization patterns observed in *S. pneumoniae* R800 and D39$_{\Delta cps}$ show that cells transition from early-division (no visible constriction at midcell) to septation (mid-division) states in which a single annular labeled region at midcell constricts progressively (Figures 2B–2D). In late-division stages, cells display the typical "butterfly" pattern resulting from active PG synthesis at parental and equatorial division sites (Figures 2B–2D).

Using these images, we measured various dimensions of the PG synthesis regions (Figure 3A). The diameter d at the parental division site, which decreases as a function of the cell length l (Figure 3B), was used as a reference for the advancement of the cell cycle. To thoroughly compare the morphology of strains R800 and D39$_{\Delta cps}$, we measured the average hemispheric length L_H and equatorial diameter D of daughter cells (Figure 3A; STAR Methods). D_{R800} was 0.80 ± 0.06 μm (SD given; n = 84) and $D_{D39\Delta cps}$ was 1.02 ± 0.13 μm (SD given; n = 92), showing that D39$_{\Delta cps}$ cells are about 1.3 times wider than R800 cells (Figures 3C and 3D). Likewise, R800 cells are shorter than D39$_{\Delta cps}$ ones as L_H values were, respectively, 0.50 ± 0.05 μm (n = 78) and 0.60 ± 0.15 μm (n = 92). Finally, for each individual cell, we calculated their elliptic ratio $E = 2L_H/D$, which reflects the global morphology of the cell. This calculation showed that D39$_{\Delta cps}$ cells are not only wider and longer but are also rounder than

Please cite this article in press as: Trouve et al., Nanoscale dynamics of peptidoglycan assembly during the cell cycle of *Streptococcus pneumoniae*, Current Biology (2021), https://doi.org/10.1016/j.cub.2021.04.041

CellPress
OPEN ACCESS

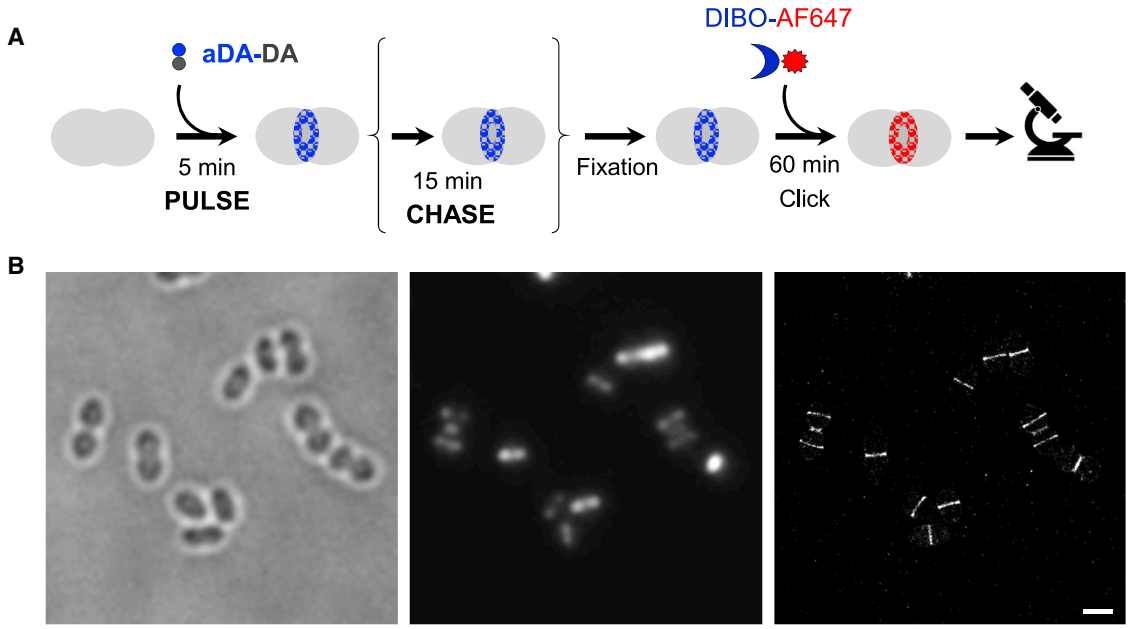

Figure 1. Labeling of pneumococcal PG with a D-Ala-D-Ala derivative for dSTORM imaging

(A) Labeling scheme to observe PG synthesis (PULSE) and its short-term fate (PULSE-CHASE) in *S. pneumoniae* cells using aDA-DA (chemical structure in Figures S1B and S1C for its incorporation into PG). The time used to pellet and resuspend the cells was not taken into account in the pulse and chase periods. (B) Large field of *S. pneumoniae* R800 cells labeled with aDA-DA. Cells in exponential growth phase were grown for 5 min in the presence of 2.5 mM aDA-DA (see Figure S2 for labeling of cells with lower amounts of aDA-DA or shorter incubation periods), fixed, and incubated with 35 μM DIBO-AF647 for fluorescent labeling. Bright-field (left panel), diffraction-limited (middle panel), and reconstructed dSTORM (right panel) images are shown. Scale bar, 1 μm.
See Figure S2 for morphological analysis and characterization of the probe incorporation pathway.

R800 cells (E_{R800} = 1.26 ± 0.13, n = 78, and $E_{D39\Delta cps}$ = 1.17 ± 0.23, n = 92).

Two successive division cycles occur simultaneously in the growing cell, and the extent of this overlap is an important morphological determinant. To quantify this phenomenon, we determined the parameter d_G, which is the parental septal diameter at which the next generation starts, marked by the presence of PG labeling at equatorial sites (Figure 3E). The ratio between d_G and the largest diameter D is smaller in R800 (d_G/D_{R800} = 0.55) than in D39$_{\Delta cps}$ cells ($d_G/D_{D39\Delta cps}$ = 0.63), showing that daughter-cell division starts earlier in the latter case and indicating a greater overlap of the generations. Consistent with this observation, we found that R800 cells display about 20% of "butterfly" localization patterns (n = 231) while those cells represent 39% of the D39$_{\Delta cps}$ population (n = 119; Figures 2C and 2D).

Dynamics of PG synthesis along the pneumococcal cell cycle

To investigate the variation of PG incorporation along the cell cycle, we quantified the number of fluorophore localizations at parental and equatorial sites. In both strains, the number of localizations increases significantly between early- and mid-division stages and decreases at the later stage (Figure 3F). This quantification constitutes an estimation, but not an absolute measure, of the amount of newly synthesized PG because fluorophore blinking introduces noise in the molecular counting process. Moreover, the amount of synthesized PG is underestimated by the fact that, after aDA-DA incorporation into PG, the aDA is subject to removal by the successive activities of the D,D-carboxypeptidase DacA and L,D-carboxypeptidase DacB, which, respectively, remove the fifth and fourth residues of the pentapeptide chain.[30,31]

Interestingly, the longitudinal width ($W_{1,2}$ or w; Figure 3A) of the labeled region tends to increase during the cell cycle in both strains (Figures 3G and 3H). Although equatorial W_1 and W_2 values do not vary with the labeling diameter, they are smaller than w values measured at later stages of the cell cycle. In addition, the longitudinal width w of the parental labeling increases as its diameter d shrinks. These observations indicate that the lengthening (growth along the longitudinal cell axis) accelerates during division. Consistent with the fact that R800 cells are more elongated than D39$_{\Delta cps}$ ones, this acceleration is more pronounced in strain R800 compared to D39$_{\Delta cps}$ (Δw_{R800} = 97.5 nm, n = 282, and $\Delta w_{D39\Delta cps}$ = 50 nm, n = 211; from early to late division stages; Figure 3I).

To get insights into the dynamics of PG synthesis along the radial axis of the cell, we observed cells held in a vertical or angled position in agarose microholes (Figure 4C).[32] In contrast with the nodal pattern recently observed for FDAA (fluorescent D-amino acid) incorporation,[18] the distribution of the dSTORM localizations was rather homogeneous (Figures 4A and 4B). This is likely due to the nature of the PG labeling probes. We used a D-Ala-D-Ala analog, which labels the growing PG through lipid II polymerization and crosslinking of the new glycan strands, while FDAAs are incorporated at the cell surface by a futile activity of the transpeptidases.[29,33] Therefore, FDAAs might be incorporated at a higher yield than aDA-DA, resulting in high

Please cite this article in press as: Trouve et al., Nanoscale dynamics of peptidoglycan assembly during the cell cycle of *Streptococcus pneumoniae*, Current Biology (2021), https://doi.org/10.1016/j.cub.2021.04.041

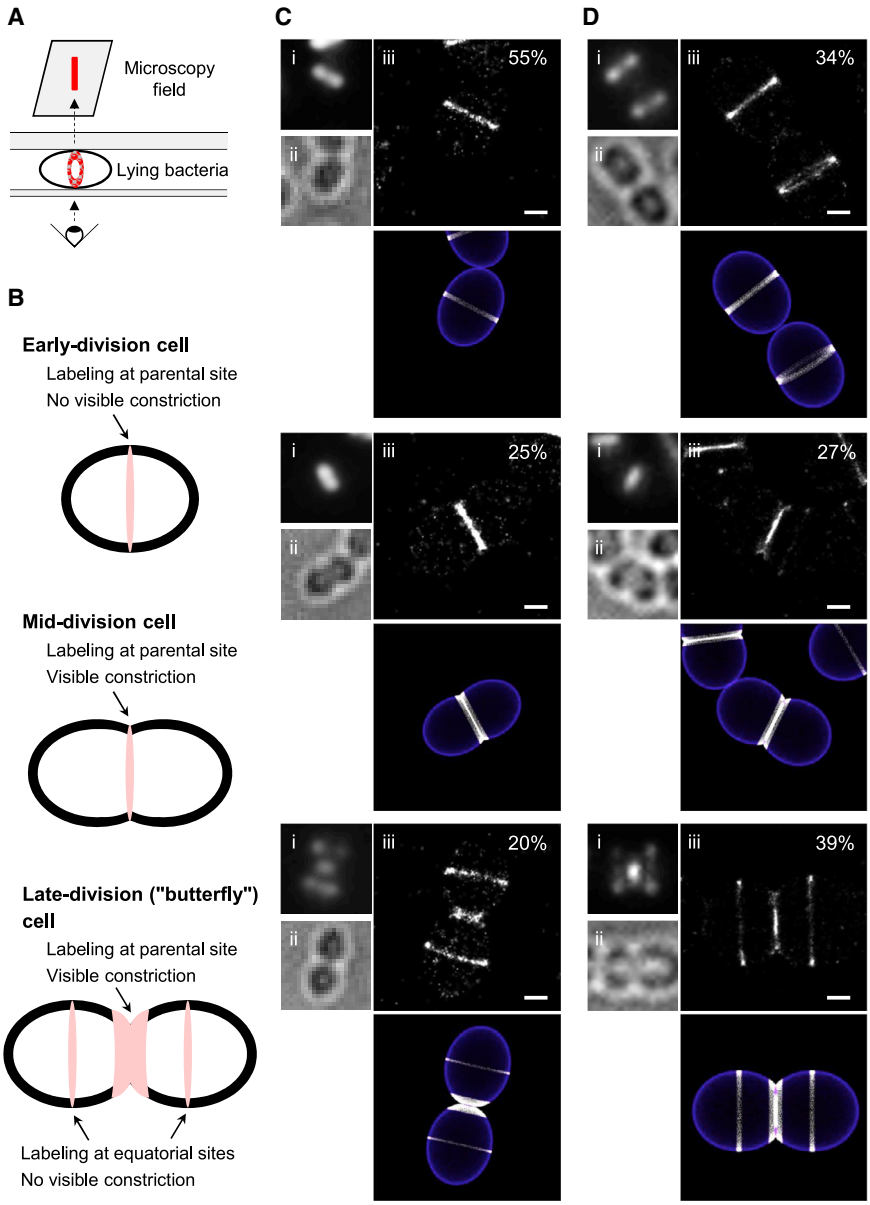

Figure 2. PG synthesis observed in the longitudinal axis of the cell

(A) Schematics showing a cell mounted between a glass slide and a coverslip, allowing a side view of the labeling pattern. In this orientation, the 2D projection of the annular labeled regions results in band-like patterns.

(B) 2D scheme of cells and PG labeling patterns at three stages of the cell cycle. Early-division cells show a single band-like labeling with no visible constriction at the parental division site. In mid-division cells, the midcell labeling is associated with visible constriction and late-division cells display a "butterfly" labeling pattern, which consists of labeling at the constricted parental site and band-like patterns with no visible constriction at the two equatorial (daughter cells) division sites.

(C and D) R800 (C) or D39$_{\Delta cps}$ (D) cells in exponential growth phase were incubated during 5 min with aDA-DA, fixed, and labeled with DIBO-AF647 before microscopy data collection. Typical diffraction-limited (i) and bright-field (ii) images, as well as reconstructed dSTORM localization patterns (iii) are shown from early- (top panels) to late- (lower panels) division stages. Scale bars, 250 nm. The number of cells measured to determine the proportion of each class is n = 231 for R800 and n = 119 for D39$_{\Delta cps}$ cells. Below each dSTORM image, the corresponding localization pattern was simulated using the geometrical model, with parameters extracted from measurements of experimental data. The blue color delineates the cell wall.

signal-to-noise ratio despite short labeling periods (~17 s). With the longer labeling pulses required with aDA-DA, possible nodal patterns might be averaged out by the movement of the PG synthases during the labeling period. In addition, FDAA labeling signals the presence of active PBPs but may not reflect their actual PG synthesis activity.

Several circular or elliptical patterns were observed, corresponding to different stages of PG synthesis (Figures 4A and 4B). Most cells (87% of the R800 population, n = 246, and 89% of D39$_{\Delta cps}$ cells, n = 176) displayed a hollow annular labeled region (Figures 4A and 4B, cells *a–c1*), whose radial width *r* (Figure 4D) increased while the outer diameter d_{out} shrank (Figures 4E and 4F) as the cell cycle progressed. In whole R800 cells imaged by transmission electron microscopy, the radial width of the septum was also found to be greater in advanced division stages (Figure S3). The small sample of electron micrographs precluded statistical analysis, but they are consistent with a previous electron microscopy study of enterococci that had revealed that the radial width of the septum increases from about 50 to 200 nm until it closes.[34] Altogether, these observations indicate that septal synthesis at the leading edge of the invaginating membrane progresses centripetally faster than peripheral splitting of the septum by PG hydrolases. As a consequence, the radial thickness of the septal plate increases until the septum closes.

Interestingly, a subset of R800 and D39$_{\Delta cps}$ cells displaying a hollow labeling pattern showed two concentric regions of high localization density separated by a narrow region of low localization density (Figures 4A and 4B, cells *c1*). The separation between the two labeled regions was more visible in D39$_{\Delta cps}$ cells (14% of cells; n = 176) compared to R800 (5%; n = 246) cells, indicating again that their dynamics of PG synthesis are slightly different. In another subset of cells (8% in R800, n = 246; 7% in D39$_{\Delta cps}$, n = 176), we could observe a full septal disk, with or without labeling at equatorial sites (Figures 4A and 4B, cells *c2*). In cells *c1*, the enzymes in charge of peripheral synthesis have not progressed enough toward the center of the division plane during the pulse period to reach the region labeled by the enzymes in charge of septal synthesis. Patterns observed in cells *c2* (as well as in cells

Please cite this article in press as: Trouve et al., Nanoscale dynamics of peptidoglycan assembly during the cell cycle of *Streptococcus pneumoniae*, Current Biology (2021), https://doi.org/10.1016/j.cub.2021.04.041

CellPress
OPEN ACCESS

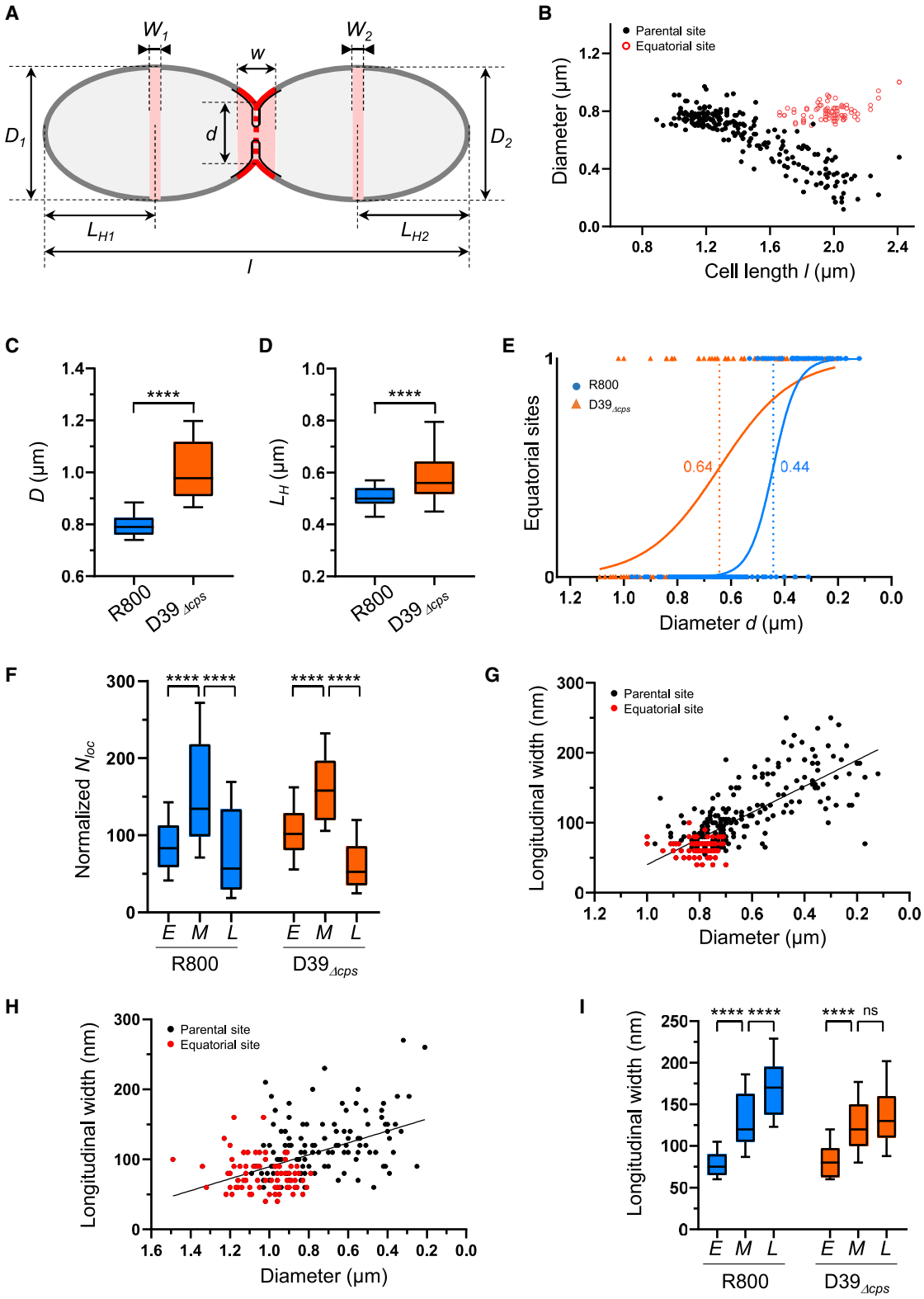

Figure 3. Analysis of localization patterns observed in the longitudinal axis of the cell

(A) Schematic representation of a pulse-labeled cell in a late-division stage, lying along its longitudinal axis and displaying a "butterfly" labeling pattern. The pink areas correspond to regions of new PG pulse-labeled with aDA-DA. The diameter of the parental labeled region at midcell (d) and at equatorial positions (D_1 and D_2), as well as the longitudinal width of those labelings (w, W_1, and W_2, respectively), the cell length (l), and the length of the two parental hemispheres (L_{H1} and L_{H2}) are shown.

(legend continued on next page)

Please cite this article in press as: Trouve et al., Nanoscale dynamics of peptidoglycan assembly during the cell cycle of *Streptococcus pneumoniae*, Current Biology (2021), https://doi.org/10.1016/j.cub.2021.04.041

a and *b*) arise if the inner diameter d_{in} at the beginning of the pulse period is equal or larger than the outer diameter d_{out} at the end of the pulse. In this case, no separation can be observed between the zones of septal and peripheral PG synthesis. The observation of the *c1* and *c2* localization profiles at mid-division indicates a certain heterogeneity in the dynamics of septal and peripheral syntheses among the cell population. Cells *c2* are designated by orange arrows in Figures S5G and S5H.

In our experiments, few late-division cells entered the microholes vertically. Nonetheless, some of these cells (2% and 1% of R800 [n = 246] and D39$_{\Delta cps}$ [n = 176] cells, respectively) displayed large nascent equatorial sites and a parental site harboring a central septal dot surrounded by an outer ring (Figures 4A and 4B, cells *d*). Again, the separation between the central localizations and the peripheral ones was more visible in D39$_{\Delta cps}$ cells. Finally, some cells with equatorial labeling (3% of R800, n = 246; 3% of D39$_{\Delta cps}$, n = 176) harbored a single small parental ring (Figures 4A and 4B, cells *e*), which likely corresponds to insertion of peripheral PG only (see the Geometrical model section below).

PBP2x and PBP2b are the two pneumococcal class B PBPs and are proposed to contribute to septal and peripheral PG synthesis, respectively.[17,19,20] Although no known specific inhibitor of PBP2b exists, the activity of PBP2x is specifically inhibited by methicillin.[35,36] When we treated D39$_{\Delta cps}$ cells with methicillin, 80% of cells (n = 614) displayed a bulged and/or elongated phenotype that was previously associated with arrest of septal synthesis.[17,19,20,35] Among those cells, 255 cells were tilted enough to observe the radial architecture of the PG synthesis region. None of them showed a double concentric labeling pattern (Figure 4G), although in the absence of methicillin, 14% of D39$_{\Delta cps}$ cells (n = 176) showed two concentric rings and 1% of cells (n = 176) displayed a central dot surrounded by an outer ring. On the other hand, we used a previously described D39$_{\Delta cps}$ strain, in which the amount of the elongasome component PBP2b is controlled from an ectopic fucose-inducible promoter, to assess the contribution of PBP2b to the labeling patterns.[17] Similar to observations with FDAA labeling,[17] depletion of PBP2b upon fucose removal (Figure S4) did not abolish double concentric rings of aDA-DA labeling (15% of cells; n = 692; Figure 4H, cells *c1* and *d*). Nevertheless, 3% of cells (n = 692) displayed very faint outer rings (Figure 4H, cell *c1'*) and 13% of cells (n = 692) did not display enriched labeling at parental division sites that are not fully constricted (Figure 4H, cell *d'*). Altogether, these observations indicate that the inner labeled region is dependent on PBP2x and that peripheral synthesis can still happen in the absence of PBP2b, even if it is somehow impaired, suggesting that it is not strictly dependent on the elongasome activity.

Evolution of newly inserted peptidoglycan during the cell cycle

To investigate the fate of the new PG, we performed pulse-chase experiments in which cells were incubated during 15 min in the absence of aDA-DA after the labeling pulse. In butterfly-displaying cells (19% of R800 cells, n = 388; 24% of D39$_{\Delta cps}$ cells, n = 229), the equatorial-labeled regions displayed double bands separated by a thin region of unlabeled PG (Figures 5A and 5B, white arrowheads in cells *c*). At these positions, PG that was pulse labeled at the onset of the new cell cycle has thus been pushed apart by unlabeled PG synthesized during the chase period. This double-band pattern was also observed in cells displaying a slight constriction (50% of R800 cells, n = 388; 55% of D39$_{\Delta cps}$ cells, n = 229; Figures 5A and 5B, cells *a*), but the distance separating the two bands was larger (Figure 5C). From nascent to slightly constricted cells, the two labeled bands not only moved away from each other but also got wider (Figure 5D). As a result of this widening, some cells showed two thick, adjacent labeled bands at later division stages (26% of R800 cells, n = 388; 11% of D39$_{\Delta cps}$ cells, n = 229; Figures 5A and 5B, cells *b2*). In other constricted cells, however, the two chased bands sandwiched a central one, resulting in a triple-band pattern (5% of R800 cells, n = 388; 10% of D39$_{\Delta cps}$ cells, n = 229; Figures 5A and 5B, cells *b1*). This pattern is consistent with the double concentric rings present in cells observed down their longitudinal axis after the pulse experiment (Figures 4A and 4B, cells *c1*). In the triple-band pattern, the central band likely corresponds to the central labeled ring that remained unsplit during the chase period while the two lateral bands would correspond to the outer labeled ring split and segregated during the chase. Consistently, the separation between the different PG synthesis regions was more pronounced in D39$_{\Delta cps}$ cells (Figures 4B, cell *c1*, and 5B, cell *b1*). This triple-band pattern was still visible at the parental division site of D39$_{\Delta cps}$ cells that were about to separate (16% of the butterfly-displaying cells; n = 56), although in R800 cells, we only observed two unsplit thick bands (Figure 5, cell *c*).

Geometrical model

To facilitate understanding of the localization patterns after labeling pulses and chases, we developed a geometrical animated

(B) Evolution of the diameter of the parental (*d*, black dots) and equatorial (D_1 and D_2, red circles) division sites as a function of the cell length *l* of R800 cells.
(C) Distribution of the largest diameters *D* among R800 (n = 84) and D39$_{\Delta cps}$ (n = 92) cell populations.
(D) Distribution of the hemisphere lengths L_H among R800 (n = 78) and D39$_{\Delta cps}$ (n = 92) cell populations.
(E) Determination of the parental diameter at which the next generation starts (d_G, dashed lines) as the inflexion point of a sigmoid fitted to the presence (value = 1) or absence (value = 0) of equatorial divisions against the parental diameter *d* in R800 (blue) and D39$_{\Delta cps}$ (orange) cells.
(F) Distributions of the number of localizations among early- (*E*), mid- (*M*), and late-divisional (*L*) R800 cells (n(*E*) = 184, n(*M*) = 53, and n(*L*) = 45 cells) and D39$_{\Delta cps}$ cells (n(*E*) = 132, n(*M*) = 32, and n(*L*) = 47 cells).
(G and H) Evolution of the longitudinal width of the parental (*w*, in black) and equatorial (W_1 and W_2, in red) labeling patterns as a function of their diameter in R800 (G; n = 282) and D39$_{\Delta cps}$ (H; n = 211) cells. The black line is a linear fitting performed on the ensemble of the data.
(I) Distributions of the longitudinal width of labeling *w* among *E*, *M*, and *L* R800 cells (n(*E*) = 184, n(*M*) = 53, and n(*L*) = 45 cells) and D39$_{\Delta cps}$ cells (n(*E*) = 132, n(*M*) = 32, and n(*L*) = 47 cells).
(C, D, F, and I) Data are represented with boxplots showing the interquartile range (10th and 90th percentile), the median value, and whiskers for minimum and maximum values. p values from the U test of Mann-Whitney between different datasets are indicated with quadruple asterisks when the observed difference is statistically significant ($p < 0.0001$) or with "ns" when no significant difference is observed ($p > 0.05$).

Please cite this article in press as: Trouve et al., Nanoscale dynamics of peptidoglycan assembly during the cell cycle of *Streptococcus pneumoniae*, Current Biology (2021), https://doi.org/10.1016/j.cub.2021.04.041

CellPress
OPEN ACCESS

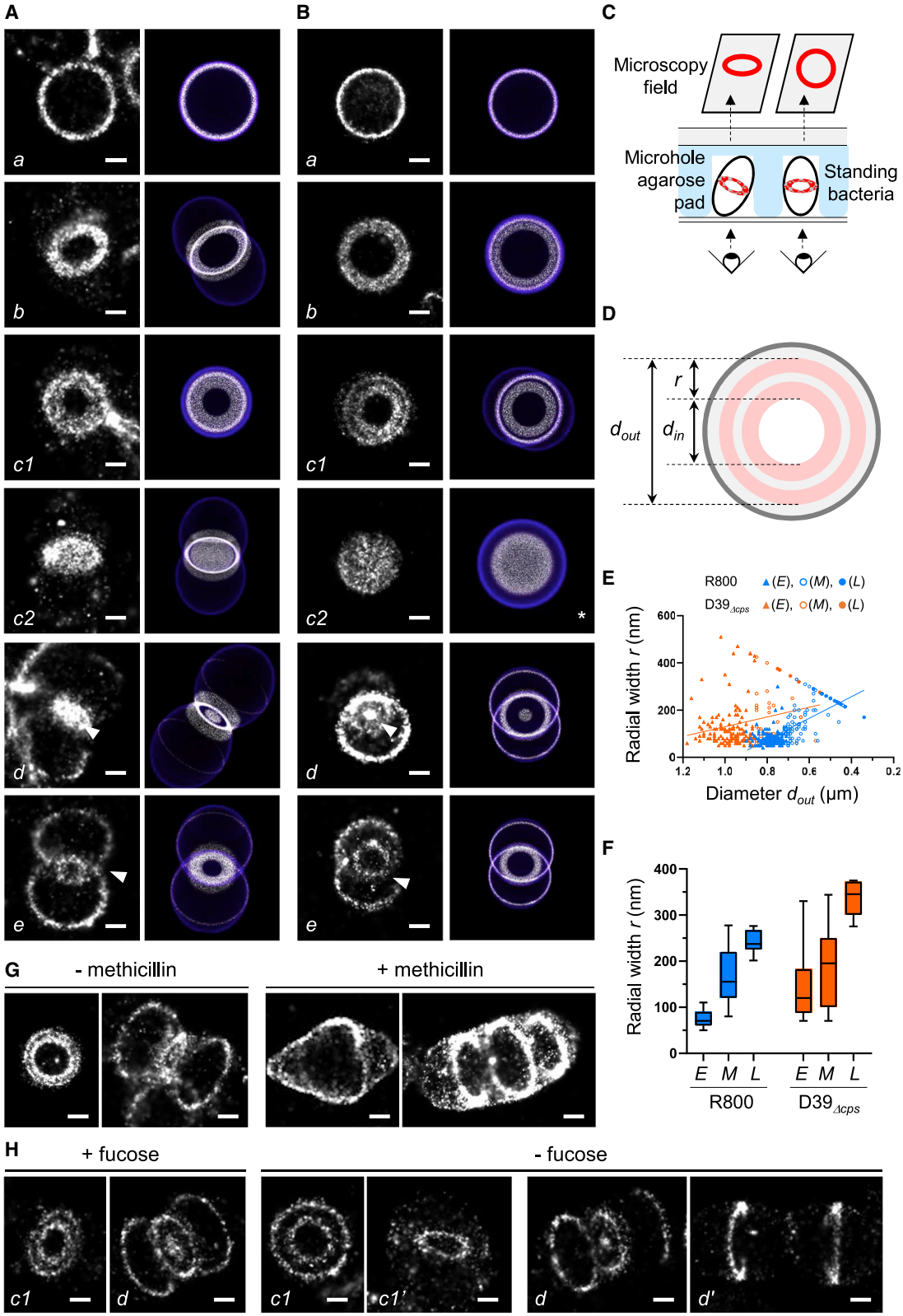

(legend on next page)

Please cite this article in press as: Trouve et al., Nanoscale dynamics of peptidoglycan assembly during the cell cycle of *Streptococcus pneumoniae*, Current Biology (2021), https://doi.org/10.1016/j.cub.2021.04.041

three-dimensional model of cell wall expansion in ovoid cells (STAR Methods). The shape of the mature cell was modeled as a prolate ellipsoid with a defined elliptic ratio ($E = L/D$). Several simplifying assumptions were made in the model. First, no elasticity or deformation was introduced in the model: once created, segments of the cell surface do not change shape. Second, the thickness and density of the PG are considered uniform. The septal disk is defined between its outer edge radius ($R_{out} = d/2$) and its inner rim radius ($R_{in} = d_{in}/2$). Points of the septal outer circle follow an elliptic trajectory to generate the ellipsoid surface. Points of the septal inner circle also follow an elliptic trajectory from the equator to the point where the septum closes. Note that, whereas the elliptic trajectory of R_{out} is imparted by the no-deformation assumption, the elliptic trajectory of R_{in} is an arbitrary *ad hoc* choice. Three adjustable parameters were introduced to allow fitting to experimental observations: (1) an acceleration factor (A), which can be imparted to the longitudinal growth; (2) the cell length at which the septum closes (C); and (3) the cell length at which the next division starts (l_G).

To model the labeling patterns, we assumed that addition of PG occurs at the leading edge (septal growth localized at d_{in}) and at the periphery (elongation occurring at d) of the septum. Accordingly, the radial or longitudinal width added during the pulse period is labeled. In addition to the three numbers that command the geometry of the growing cell wall at given stages of the cell cycle, the beginning and duration of the labeling pulses (P) can be defined to model the labeling patterns.

To determine the combination of factors that best reproduce the observation, we analyzed the measurements of experimental data as detailed in the STAR Methods section and Figures S5A–S5F. Based on parameters extracted from experimental measurements (Table S1), an ellipsoid model in which both septal and peripheral synthesis start from the beginning of the cell cycle and in which peripheral synthesis persists after septum closure accounts remarkably well with the experimental complex patterns (Figures 2, 4, and 5; Videos S1 and S2). However, because the model parameters define the morphological trajectory of an "average cell," individual cells may follow significantly different dynamics, as evidenced by the spread of the measurements around the fitted curves (Figures S5G–S5J).

DISCUSSION

In ovococci, experiments in which PG is labeled at different time points show that PG is synthesized at midcell to later become lateral and form the new hemisphere in each daughter cell.[37] The literature suggests that this process involves two modes of PG synthesis, called septal and peripheral synthesis, respectively associated with cell division (septum formation) and elongation and respectively carried out by the divisome and elongasome machineries.[13–16,38] In the pneumococcus, the existence of a divisome and an elongasome was first suggested by the presence of essential class B PBP/SEDS pairs specifically required for division and elongation in rod-shaped bacteria: PBP2x/FtsW and PBP2b/RodA.[39,40] This idea was further supported by division and elongation defects observed when the activity of PBP2x or PBP2b was impaired, respectively.[19–21] Elongated and lenticular phenotypes indicate that septation and elongation can somehow be uncoupled, suggesting that the divisome and the elongasome have independent activities. In this context, ovococci morphogenesis has often been discussed in terms of a switch or transition from peripheral to septal synthesis.[13–16]

However, several observations hardly fit with this model, including the facts that (1) PBPs in charge of septal (PBP2x) and peripheral (PBP2b) synthesis arrive concomitantly at new division sites;[17] (2) PBP2x inactivation in pre-divisional cells results in midcell bulging;[20] (3) slight invaginations are observed at equatorial positions, suggestive of septal synthesis at a very early stage of the cell cycle (Figure S3 and Higgins and Shockman[34]); and (4) double concentric rings of FDAA labeling are observed at early stages.[18]

The dSTORM data reported here provide evidence for a mechanism that differs from alternations between a phase of peripheral synthesis and a phase of septal synthesis coupled to splitting of the septum. In particular, the pulse-chase observations

Figure 4. PG synthesis observed in the radial axis of the cell

(A and B) Typical dSTORM localization patterns of new PG in cells trapped vertically or at an angle in microholes. Early- to late-division stages are shown from top to bottom panels. Exponentially growing R800 (A) and D39$_{\Delta cps}$ (B) cells were incubated for 5 min with 2.5 mM aDA-DA, fixed, and labeled with DIBO-AF647 before being loaded into microhole agarose pads. Next to each dSTORM image, the corresponding localization pattern was simulated using the geometrical model. The blue color delineates the cell wall. The asterisk signals a localization pattern that lies outside the average morphological path and required manual tuning of the parameters. An animation leading to pattern Be is shown as Video S1.

(C) Schematics showing cells trapped in microholes, allowing an elliptic or annular top view of the labeling.

(D) Schematic representation of a mid-division cell, observed down its longitudinal axis. The outer (d_{out}) and inner (d_{in}) diameters of the labeling, as well as its radial width (r), are shown.

(E) Evolution of the radial width of labeling (r) of the septal plate as a function of the outer diameter d_{out} in R800 (blue; n = 238) and D39$_{\Delta cps}$ (orange; n = 171) cells. Cells *e* were excluded from the graph as their labeling most likely results from peripheral synthesis. The lines are linear fittings of the data. Symbols correspond to groups of cells defined in (F).

(F) Distribution of the radial width of labeling (r) in *E*, *M*, and *L* R800 (n(*E*) = 158, n(*M*) = 64, and n(*L*) = 16 cells) and D39$_{\Delta cps}$ (n(*E*) = 134, n(*M*) = 32, and n(*L*) = 5 cells) cells. The E, M, and L groups were binned based on the outer diameter (d_{out}) ($d_{out}(E)$ = 0.90–0.70 μm for R800, $d_{out}(E)$ = 1.18–0.85 μm for D39$_{\Delta cps}$; $d_{out}(M)$ = 0.70–0.46 μm for R800, $d_{out}(M)$ = 0.85–0.64 μm for D39$_{\Delta cps}$; $d_{out}(L)$ = 0.59–0.30 μm for R800, $d_{out}(L)$ = 0.75–0.47 μm for D39$_{\Delta cps}$). Data are represented with boxplots showing the interquartile range (10th and 90th percentile), the median value, and whiskers for minimum and maximum values. See Figure S3 for observation of the radial width of the septal plate by transmission electron microscopy.

(G) dSTORM images of exponentially growing D39$_{\Delta cps}$ cells incubated without (left panels) or with 0.3 μg×mL^{-1} methicillin (right panels) for 1 h before labeling with aDA-DA and DIBO-AF647.

(H) dSTORM images of exponentially growing cells of *S. pneumoniae* strain IU7397 (D39$_{\Delta cps}$ *Δpbp2b bgaA::P$_{fcsK}$-pbp2b*) grown with (left panels) or without 2% fucose (right panels) before labeling with aDA-DA and DIBO-AF647. Scale bars throughout, 250 nm. See Figure S4 for immunoblot analysis of PBP2b depletion in D39$_{\Delta cps}$ cells.

Please cite this article in press as: Trouve et al., Nanoscale dynamics of peptidoglycan assembly during the cell cycle of *Streptococcus pneumoniae*, Current Biology (2021), https://doi.org/10.1016/j.cub.2021.04.041

CellPress
OPEN ACCESS

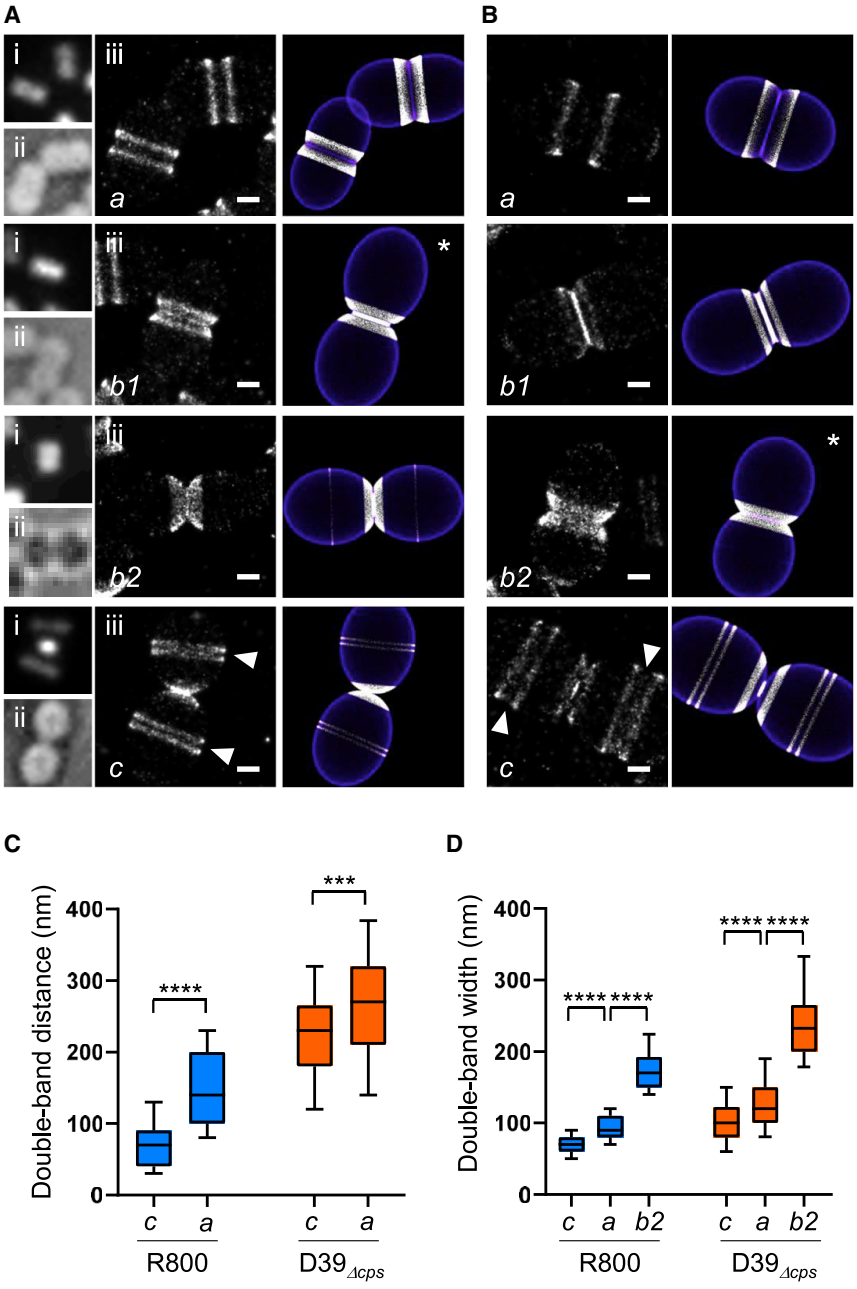

Figure 5. Evolution of the new PG along the pneumococcal cell cycle

(A and B) Exponentially growing R800 (A) and D39$_{\Delta cps}$ (B) cells were incubated for 5 min with 2.5 mM aDA-DA (pulse), grown for 15 min in the absence of the probe (chase), fixed, and labeled with DIBO-AF647 before dSTORM data collection. Diffraction-limited (i) and bright field (ii) images, as well as reconstructed dSTORM localization patterns (iii) are shown. Early- to late-division stages are shown from top to bottom. The white arrowheads point at equatorial double-band patterns. Scale bars, 250 nm. On the right of each dSTORM image, the corresponding localization pattern was simulated *in silico*. An animation leading to pattern Bc is shown as Video S2. Asterisks signal that the model parameters were adjusted manually.

(C) Distributions of the distance separating the double bands observed in cells of type *a* and *c* in (A) and (B) (R800, n(*a*) = 194 and n(*c*) = 72 cells; D39$_{\Delta cps}$, n(*a*) = 125 and n(*c*) = 56 cells).

(D) Distributions of the longitudinal width of the double bands observed in cells of type *a*, *b2*, and *c* in (A) and (B) (R800, n(*a*) = 194, n(*b2*) = 101, and n(*c*) = 72 cells; D39$_{\Delta cps}$, n(*a*) = 125, n(*b2*) = 26, and n(*c*) = 56 cells).

(C and D) Data are represented with boxplots showing the interquartile range (10th and 90th percentile), the median value, and whiskers for minimum and maximum values. p values from the U test of Mann-Whitney between different datasets are indicated with triple or quadruple asterisks when the observed differences are statistically significant with $p < 0.001$ or $p < 0.0001$, respectively.

support the idea that septal PG is split all along the cell cycle. Indeed, one would expect the combined longitudinal width of the two chased bands to equal the longitudinal width of the pulse pattern if, at the beginning of the cell cycle, the cell would grow from peripheral synthesis only. The fact that the chased labeled regions are larger than the pulse-labeled bands (Figures 2, 3, and 5) suggests that this double-band pattern includes splitting of septal PG. Additionally, and in further support of this hypothesis, the increase in the longitudinal width of these double bands parallels the continuous increase in the radial width of the septal plate. These data are therefore consistent with a model in which septal PG is synthesized all along the early- and mid-stages of the cell cycle and continuously split by hydrolases to become lateral wall, in which peripheral PG is inserted (Figure 6). In this model, a septum can only form if the cleavage speed of the septal PG is lower than its centripetal growth. If this difference of speed is slight, little or no septum will be visible at the beginning of the cell cycle and septal and peripheral syntheses will be spatially very close. This hypothesis is supported by electron microscopy images showing only slight invaginations at equatorial positions (Figure S3) and by dSTORM images showing no visible separation of the two synthesis sites at the current spatial and temporal resolution (Figures 4, cells *a* and *b*, and 5, cells *a* and equatorial positions of cells *c*). Nonetheless, as the cell cycle progresses, the splitting hydrolases and peripheral synthases increasingly lag behind the septal synthases, allowing septum formation and a separation between the septal and peripheral activities that reaches the resolution power of the dSTORM approach. Consistent with this concept, septal and peripheral PG synthesis activities can be resolved as two concentric rings at one point in the cell cycle (Figures 4 and 5).

Although this work improves our understanding of PG synthesis and remodeling in ovococci, the contribution of the various morphogenetic proteins to these processes remains partially

Please cite this article in press as: Trouve et al., Nanoscale dynamics of peptidoglycan assembly during the cell cycle of *Streptococcus pneumoniae*, Current Biology (2021), https://doi.org/10.1016/j.cub.2021.04.041

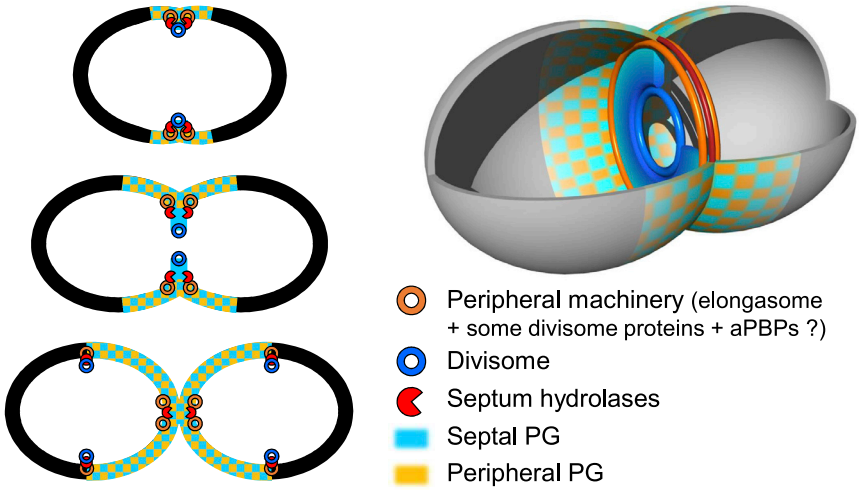

Figure 6. Illustration of PG assembly and remodeling in ovococci

Left panels: two-dimensional scheme of PG synthesis and processing at three main stages of the ovoid cell cycle. At the beginning of the cell cycle, the divisome (blue ring) localized at the leading edge of the invaginating membrane synthesizes septal PG (blue areas), which is promptly cleaved by PG hydrolases (red pac mans), precluding significant septum formation. The peripheral machinery (orange rings), which includes the elongasome, some divisome proteins, and possibly class A PBPs (aPBPs), adds peripheral PG (orange areas) within the cleaved septal layers, resulting in lateral wall made of a composite of septal and peripheral PG. As septal PG is cleaved at a lower centripetal speed than it is synthesized, a visible septum forms progressively, and the peripheral synthesis machinery lags behind the divisome. At the end of the cell cycle, the septum is closed but continues to be remodeled by PG hydrolases and the peripheral machinery until daughter cell separation. Right panel: three-dimensional illustration of a mid-division stage is shown, in which the septum is colored with a blue gradient, with darker shades corresponding to young PG and lighter shades to older material. The peripheral machinery (orange rings) adds peripheral PG (orange areas) within the septal layers cleaved by the PG hydrolases (red ring).

unclear. To tackle this, we specifically inhibited PBP2x using methicillin and observed bulged and elongated cells, all lacking small septal labeled rings or dots. These observations support the idea that the inner region in double concentric labeling patterns depends on septal synthesis performed by the divisome component PBP2x (Figure 4; Tsui et al.[17]). Cleavage of septal PG involves the putative endopeptidase/amidase PcsB, whose mild depletion results in cell separation defects.[41,42] Moreover, the rounder cell phenotype upon severe depletion of PcsB suggests that it might also cleave bonds within septal PG to allow insertion of peripheral material. The spherical phenotype of cells depleted for MltG also points to this putative lytic transglycosylase as a candidate for limited PG cleavage required for peripheral PG insertion.[43] The identity of the PG hydrolase(s) that cleave the PG network to allow insertion of additional material remains enigmatic, but it is tempting to propose that PcsB and MltG are involved, and this should be tested in the future. Regarding peripheral synthesis, the elongasome appears to be an obvious candidate machinery because pneumococcal cells deficient for PBP2b, RodA, MreC, or MreD form lentil-shaped cells.[21] Double concentric labeling patterns are, however, still observed when PBP2b is depleted (15%; n = 692), although some cells (3%; n = 692) show impaired outer labeling and others (13%; n = 692) lack enriched parental labeling in late-division stages (Figure 4H; Tsui et al.[17]). In addition, PBP2x was recently shown to remain partially localized at the periphery of the septum, and septal PG is known to be modified by class A PBPs.[18,44] Altogether, these findings suggest that the elongasome, some divisome components, and class A PBPs might all contribute to insertion of peripheral PG at the septal cleavage site.

The absence of labeling in between the two concentric labeled regions is due to septal material that was synthesized prior to the labeling period. It reveals that no or little material is inserted in this region or, in other words, that PG synthesis happens mostly at the leading edge and periphery of the septum. This pattern was more difficult to discern in R800 than in D39$_{\Delta cps}$ cells. This difference could arise if some PG is added on the whole surface of the septum in R800, but not in D39$_{\Delta cps}$. Because morphological differences between the two strains have been linked to differences in the gene encoding the class A PBP1a,[45] it will be interesting to determine the contribution of this protein, and other class A PBPs, to the localization patterns.

A major observation from the pulse labeling experiment is the increase of the longitudinal width of labeling (w) as cells progress in their division (Figures 2 and 3). This signals an acceleration of the cell lengthening that should, however, not be interpreted as an acceleration of PG synthesis because it depends on the combination of the septum splitting rate, peripheral synthesis rate, and viewing angle. Indeed, the labeling width w, which results from the projection of a curved surface on a plane perpendicular to the viewing axis, closely reflects the almost longitudinal labeled lateral surface at the beginning of the cell cycle (viewing angle $\sim 90^{\circ}$) but is significantly shorter than the highly curved and almost perpendicular labeled lateral surface at the end of the division (viewing angle $\sim 0^{\circ}$). To examine the rate of PG assembly, we investigated the relationship between the amount of PG insertion (proxied by the number of dSTORM localizations) and the surface area production using our geometrical model. This analysis reveals that the rise and decline of PG incorporation varies roughly like the rate of surface generation calculated from the model, where the variation is dominated by septal synthesis (Figure S6; STAR Methods). It is important to note that our model does not take into account PG elasticity[46,47] and assumes that PG has a uniform thickness and density (STAR Methods). Significant deviations from these assumptions could render spurious the striking correlation between the new surface area and the dSTORM localization counts.

In conclusion, the new strategy of metabolic labeling combined with dSTORM and *in silico* modeling has allowed the refined description of PG assembly in the pneumococcus. Our data are consistent with a model in which septal PG synthesized

by the divisome would be constantly split by PG hydrolases and completed by the elongasome but also possibly some divisome proteins and class A PBPs located at the periphery of the septum (Figure 6). The relative specific activities of these morphogenetic components would determine septum formation and the elliptic ratio of the cell, and our data suggest that slight differences in these activities between different strains might explain variations in the shape and size of the ovoid cells. The approach described in this work lays foundations for testing this model through detailed characterization of shape mutants and morphological effects of drugs.

STAR★METHODS

Detailed methods are provided in the online version of this paper and include the following:

- KEY RESOURCES TABLE
- RESOURCE AVAILABILITY
  - Lead contact
  - Materials availability
  - Data and code availability
- EXPERIMENTAL MODEL AND SUBJECT DETAILS
- METHOD DETAILS
  - Preparation of PG labeling reagents
  - PG labeling in S. pneumoniae cells
  - Sacculi preparation
  - Conventional optical microscopy
  - dSTORM setup and acquisition method
  - dSTORM image reconstruction
  - Measurement of the labeling patterns
  - Cryo-electron microscopy (cryo-EM)
  - Geometrical model of cell growth and labeling
  - Determination of the geometrical parameters
  - Surface area considerations
- QUANTIFICATION AND STATISTICAL ANALYSIS

SUPPLEMENTAL INFORMATION

Supplemental information can be found online at https://doi.org/10.1016/j.cub.2021.04.041.

ACKNOWLEDGMENTS

We thank members of the Vernet and Bourgeois laboratories for advice and encouragement; O. Glushonkov, J.P. Kleman, and S. Dufour for advice and support regarding dSTORM; G. Schoehn for electron microscopy; L. Espinosa for preliminary tests performed on the IMM Microscopy platform; and M. Winkler for the D39$_{\Delta cps}$ strains. Support for this work comes from the Agence Nationale de la Recherche (ANR-16-CE11-0016 to C.M., ANR-19-CE15-0011 to C.G., and Labex ARCANE ANR-17-EURE-0003 to Y.-S.W.). This work used the platforms of the Grenoble Instruct-ERIC Centre (ISBG; UMS 3518 CNRS-CEA-UGA-EMBL) within the Grenoble Partnership for Structural Biology (PSB), supported by FRISBI (ANR-10-INBS-05-02) and GRAL, financed within the University Grenoble Alpes graduate school (Ecoles Universitaires de Recherche) CBH-EUR-GS (ANR-17-EURE-0003). The electron microscope facility is supported by the Auvergne-Rhône-Alpes region, the Fondation pour la Recherche Médicale (FRM), the fonds FEDER, and the GIS-Infrastructures en Biologie Santé et Agronomie (IBISA). IBS acknowledges integration into the Interdisciplinary Research Institute of Grenoble (IRIG, CEA).

AUTHOR CONTRIBUTIONS

J.T., A.Z., Y.-S.W., and C.M. designed research; J.T., C.A., C.D., A.M.D.G., A.P., and Y.-S.W. performed experiments; J.T., A.Z., C.D., D.B., Y.-S.W., and C.M. analyzed data; B.S. provided micropillars; J.T., A.Z., and C.M. wrote the manuscript; and J.T., C.G., D.B., Y.-S.W., A.Z., and C.M. revised the manuscript.

DECLARATION OF INTERESTS

The authors declare no competing interests.

INCLUSION AND DIVERSITY

While citing references scientifically relevant for this work, we also actively worked to promote gender balance in our reference list.

Received: November 2, 2020
Revised: March 9, 2021
Accepted: April 16, 2021
Published: May 13, 2021

REFERENCES

1. Vollmer, W., Blanot, D., and de Pedro, M.A. (2008). Peptidoglycan structure and architecture. FEMS Microbiol. Rev. *32*, 149–167.
2. Barreteau, H., Kovač, A., Boniface, A., Sova, M., Gobec, S., and Blanot, D. (2008). Cytoplasmic steps of peptidoglycan biosynthesis. FEMS Microbiol. Rev. *32*, 168–207.
3. Meeske, A.J., Riley, E.P., Robins, W.P., Uehara, T., Mekalanos, J.J., Kahne, D., Walker, S., Kruse, A.C., Bernhardt, T.G., and Rudner, D.Z. (2016). SEDS proteins are a widespread family of bacterial cell wall polymerases. Nature *537*, 634–638.
4. Sauvage, E., Kerff, F., Terrak, M., Ayala, J.A., and Charlier, P. (2008). The penicillin-binding proteins: structure and role in peptidoglycan biosynthesis. FEMS Microbiol. Rev. *32*, 234–258.
5. Vollmer, W., Joris, B., Charlier, P., and Foster, S. (2008). Bacterial peptidoglycan (murein) hydrolases. FEMS Microbiol. Rev. *32*, 259–286.
6. den Blaauwen, T., de Pedro, M.A., Nguyen-Distèche, M., and Ayala, J.A. (2008). Morphogenesis of rod-shaped sacculi. FEMS Microbiol. Rev. *32*, 321–344.
7. Zapun, A., Noirclerc-Savoye, M., Helassa, N., and Vernet, T. (2012). Peptidoglycan assembly machines: the biochemical evidence. Microb. Drug Resist. *18*, 256–260.
8. Typas, A., Banzhaf, M., Gross, C.A., and Vollmer, W. (2011). From the regulation of peptidoglycan synthesis to bacterial growth and morphology. Nat. Rev. Microbiol. *10*, 123–136.
9. Daniel, R.A., and Errington, J. (2003). Control of cell morphogenesis in bacteria: two distinct ways to make a rod-shaped cell. Cell *113*, 767–776.
10. Philippe, J., Vernet, T., and Zapun, A. (2014). The elongation of ovococci. Microb. Drug Resist. *20*, 215–221.
11. Fleurie, A., Manuse, S., Zhao, C., Campo, N., Cluzel, C., Lavergne, J.-P., Freton, C., Combet, C., Guiral, S., Soufi, B., et al. (2014). Interplay of the serine/threonine-kinase StkP and the paralogs DivIVA and GpsB in pneumococcal cell elongation and division. PLoS Genet. *10*, e1004275.
12. Morlot, C., Zapun, A., Dideberg, O., and Vernet, T. (2003). Growth and division of Streptococcus pneumoniae: localization of the high molecular weight penicillin-binding proteins during the cell cycle. Mol. Microbiol. *50*, 845–855.
13. Vollmer, W., Massidda, O., and Tomasz, A. (2019). The cell wall of *Streptococcus pneumoniae*. Microbiol. Spectr. *7*. https://doi.org/10.1128/microbiolspec.GPP3-0018-2018.
14. Massidda, O., Nováková, L., and Vollmer, W. (2013). From models to pathogens: how much have we learned about Streptococcus pneumoniae cell division? Environ. Microbiol. *15*, 3133–3157.

15. Zapun, A., Vernet, T., and Pinho, M.G. (2008). The different shapes of cocci. FEMS Microbiol. Rev. *32*, 345–360.

16. Pinho, M.G., Kjos, M., and Veening, J.-W. (2013). How to get (a)round: mechanisms controlling growth and division of coccoid bacteria. Nat. Rev. Microbiol. *11*, 601–614.

17. Tsui, H.T., Boersma, M.J., Vella, S.A., Kocaoglu, O., Kuru, E., Peceny, J.K., Carlson, E.E., VanNieuwenhze, M.S., Brun, Y.V., Shaw, S.L., and Winkler, M.E. (2014). Pbp2x localizes separately from Pbp2b and other peptidoglycan synthesis proteins during later stages of cell division of Streptococcus pneumoniae D39. Mol. Microbiol. *94*, 21–40.

18. Perez, A.J., Boersma, M.J., Bruce, K.E., Lamanna, M.M., Shaw, S.L., Tsui, H.T., Taguchi, A., Carlson, E.E., VanNieuwenhze, M.S., and Winkler, M.E. (2020). Organization of peptidoglycan synthesis in nodes and separate rings at different stages of cell division of Streptococcus pneumoniae. Mol. Microbiol. Published online December 2, 2020. https://doi.org/10.1111/mmi.14659.

19. Berg, K.H., Stamsås, G.A., Straume, D., and Håvarstein, L.S. (2013). Effects of low PBP2b levels on cell morphology and peptidoglycan composition in Streptococcus pneumoniae R6. J. Bacteriol. *195*, 4342–4354.

20. Philippe, J., Gallet, B., Morlot, C., Denapaite, D., Hakenbeck, R., Chen, Y., Vernet, T., and Zapun, A. (2015). Mechanism of β-lactam action in Streptococcus pneumoniae: the piperacillin paradox. Antimicrob. Agents Chemother. *59*, 609–621.

21. Straume, D., Stamsås, G.A., Berg, K.H., Salehian, Z., and Håvarstein, L.S. (2017). Identification of pneumococcal proteins that are functionally linked to penicillin-binding protein 2b (PBP2b). Mol. Microbiol. *103*, 99–116.

22. Jacq, M., Adam, V., Bourgeois, D., Moriscot, C., Di Guilmi, A.M., Vernet, T., and Morlot, C. (2015). Remodeling of the Z-ring nanostructure during the Streptococcus pneumoniae cell cycle revealed by photoactivated localization microscopy. MBio *6*, e01108–e01115.

23. Liechti, G.W., Kuru, E., Hall, E., Kalinda, A., Brun, Y.V., VanNieuwenhze, M., and Maurelli, A.T. (2014). A new metabolic cell-wall labelling method reveals peptidoglycan in *Chlamydia trachomatis*. Nature *506*, 507–510.

24. van de Linde, S., Löschberger, A., Klein, T., Heidbreder, M., Wolter, S., Heilemann, M., and Sauer, M. (2011). Direct stochastic optical reconstruction microscopy with standard fluorescent probes. Nat. Protoc. *6*, 991–1009.

25. Rued, B.E., Zheng, J.J., Mura, A., Tsui, H.T., Boersma, M.J., Mazny, J.L., Corona, F., Perez, A.J., Fadda, D., Doubravová, L., et al. (2017). Suppression and synthetic-lethal genetic relationships of ΔgpsB mutations indicate that GpsB mediates protein phosphorylation and penicillin-binding protein interactions in Streptococcus pneumoniae D39. Mol. Microbiol. *103*, 931–957.

26. Cleverley, R.M., Rutter, Z.J., Rismondo, J., Corona, F., Tsui, H.T., Alatawi, F.A., Daniel, R.A., Halbedel, S., Massidda, O., Winkler, M.E., and Lewis, R.J. (2019). The cell cycle regulator GpsB functions as cytosolic adaptor for multiple cell wall enzymes. Nat. Commun. *10*, 261.

27. Hammond, L.R., White, M.L., and Eswara, P.J. (2019). ¸vIVA la DivIVA! J. Bacteriol. *201*, e00245–19.

28. Batson, S., de Chiara, C., Majce, V., Lloyd, A.J., Gobec, S., Rea, D., Fülöp, V., Thoroughgood, C.W., Simmons, K.J., Dowson, C.G., et al. (2017). Inhibition of D-Ala:D-Ala ligase through a phosphorylated form of the antibiotic D-cycloserine. Nat. Commun. *8*, 1939.

29. Kuru, E., Radkov, A., Meng, X., Egan, A., Alvarez, L., Dowson, A., Booher, G., Breukink, E., Roper, D.I., Cava, F., et al. (2019). Mechanisms of incorporation for D-amino acid probes that target peptidoglycan biosynthesis. ACS Chem. Biol. *14*, 2745–2756.

30. Barendt, S.M., Sham, L.-T., and Winkler, M.E. (2011). Characterization of mutants deficient in the L,D-carboxypeptidase (DacB) and WalRK (VicRK) regulon, involved in peptidoglycan maturation of Streptococcus pneumoniae serotype 2 strain D39. J. Bacteriol. *193*, 2290–2300.

31. Morlot, C., Pernot, L., Le Gouellec, A., Di Guilmi, A.M., Vernet, T., Dideberg, O., and Dessen, A. (2005). Crystal structure of a peptidoglycan synthesis regulatory factor (PBP3) from Streptococcus pneumoniae. J. Biol. Chem. *280*, 15984–15991.

32. Söderström, B., Chan, H., Shilling, P.J., Skoglund, U., and Daley, D.O. (2018). Spatial separation of FtsZ and FtsN during cell division. Mol. Microbiol. *107*, 387–401.

33. Kuru, E., Hughes, H.V., Brown, P.J., Hall, E., Tekkam, S., Cava, F., de Pedro, M.A., Brun, Y.V., and VanNieuwenhze, M.S. (2012). In Situ probing of newly synthesized peptidoglycan in live bacteria with fluorescent D-amino acids. Angew. Chem. Int. Ed. Engl. *51*, 12519–12523.

34. Higgins, M.L., and Shockman, G.D. (1976). Study of cycle of cell wall assembly in Streptococcus faecalis by three-dimensional reconstructions of thin sections of cells. J. Bacteriol. *127*, 1346–1358.

35. Land, A.D., Tsui, H.-C.T., Kocaoglu, O., Vella, S.A., Shaw, S.L., Keen, S.K., Sham, L.-T., Carlson, E.E., and Winkler, M.E. (2013). Requirement of essential Pbp2x and GpsB for septal ring closure in Streptococcus pneumoniae D39. Mol. Microbiol. *90*, 939–955.

36. Kocaoglu, O., Tsui, H.-C.T., Winkler, M.E., and Carlson, E.E. (2015). Profiling of β-lactam selectivity for penicillin-binding proteins in Streptococcus pneumoniae D39. Antimicrob. Agents Chemother. *59*, 3548–3555.

37. Hsu, Y.-P., Rittichier, J., Kuru, E., Yablonowski, J., Pasciak, E., Tekkam, S., Hall, E., Murphy, B., Lee, T.K., Garner, E.C., et al. (2017). Full color palette of fluorescent d-amino acids for *in situ* labeling of bacterial cell walls. Chem. Sci. (Camb.) *8*, 6313–6321.

38. Pérez-Núñez, D., Briandet, R., David, B., Gautier, C., Renault, P., Hallet, B., Hols, P., Carballido-López, R., and Guédon, E. (2011). A new morphogenesis pathway in bacteria: unbalanced activity of cell wall synthesis machineries leads to coccus-to-rod transition and filamentation in ovococci. Mol. Microbiol. *79*, 759–771.

39. Gérard, P., Vernet, T., and Zapun, A. (2002). Membrane topology of the Streptococcus pneumoniae FtsW division protein. J. Bacteriol. *184*, 1925–1931.

40. Goffin, C., and Ghuysen, J.M. (1998). Multimodular penicillin-binding proteins: an enigmatic family of orthologs and paralogs. Microbiol. Mol. Biol. Rev. *62*, 1079–1093.

41. Bartual, S.G., Straume, D., Stamsås, G.A., Muñoz, I.G., Alfonso, C., Martínez-Ripoll, M., Håvarstein, L.S., and Hermoso, J.A. (2014). Structural basis of PcsB-mediated cell separation in Streptococcus pneumoniae. Nat. Commun. *5*, 3842.

42. Sham, L.-T., Barendt, S.M., Kopecky, K.E., and Winkler, M.E. (2011). Essential PcsB putative peptidoglycan hydrolase interacts with the essential FtsXSpn cell division protein in Streptococcus pneumoniae D39. Proc. Natl. Acad. Sci. USA *108*, E1061–E1069.

43. Tsui, H.-C.T., Zheng, J.J., Magallon, A.N., Ryan, J.D., Yunck, R., Rued, B.E., Bernhardt, T.G., and Winkler, M.E. (2016). Suppression of a deletion mutation in the gene encoding essential PBP2b reveals a new lytic transglycosylase involved in peripheral peptidoglycan synthesis in Streptococcus pneumoniae D39. Mol. Microbiol. *100*, 1039–1065.

44. Straume, D., Piechowiak, K.W., Olsen, S., Stamsås, G.A., Berg, K.H., Kjos, M., Heggenhougen, M.V., Alcorlo, M., Hermoso, J.A., and Håvarstein, L.S. (2020). Class A PBPs have a distinct and unique role in the construction of the pneumococcal cell wall. Proc. Natl. Acad. Sci. USA *117*, 6129–6138.

45. Lanie, J.A., Ng, W.-L., Kazmierczak, K.M., Andrzejewski, T.M., Davidsen, T.M., Wayne, K.J., Tettelin, H., Glass, J.I., and Winkler, M.E. (2007). Genome sequence of Avery's virulent serotype 2 strain D39 of Streptococcus pneumoniae and comparison with that of unencapsulated laboratory strain R6. J. Bacteriol. *189*, 38–51.

46. Boulbitch, A., Quinn, B., and Pink, D. (2000). Elasticity of the rod-shaped gram-negative eubacteria. Phys. Rev. Lett. *85*, 5246–5249.

47. Koch, A.L., and Woeste, S. (1992). Elasticity of the sacculus of Escherichia coli. J. Bacteriol. *174*, 4811–4819.

48. Lefevre, J.C., Claverys, J.P., and Sicard, A.M. (1979). Donor deoxyribonucleic acid length and marker effect in pneumococcal transformation. J. Bacteriol. *138*, 80–86.

49. Schneider, C.A., Rasband, W.S., and Eliceiri, K.W. (2012). NIH Image to ImageJ: 25 years of image analysis. Nat. Methods *9*, 671–675.

50. Schindelin, J., Arganda-Carreras, I., Frise, E., Kaynig, V., Longair, M., Pietzsch, T., Preibisch, S., Rueden, C., Saalfeld, S., Schmid, B., et al. (2012). Fiji: an open-source platform for biological-image analysis. Nat. Methods *9*, 676–682.

51. Ovesný, M., Křížek, P., Borkovec, J., Svindrych, Z., and Hagen, G.M. (2014). ThunderSTORM: a comprehensive ImageJ plug-in for PALM and STORM data analysis and super-resolution imaging. Bioinformatics *30*, 2389–2390.

52. Lacks, S., and Hotchkiss, R.D. (1960). A study of the genetic material determining an enzyme in Pneumococcus. Biochim. Biophys. Acta *39*, 508–518.

53. Nieuwenhuizen, R.P.J., Lidke, K.A., Bates, M., Puig, D.L., Grünwald, D., Stallinga, S., and Rieger, B. (2013). Measuring image resolution in optical nanoscopy. Nat. Methods *10*, 557–562.

Please cite this article in press as: Trouve et al., Nanoscale dynamics of peptidoglycan assembly during the cell cycle of *Streptococcus pneumoniae*, Current Biology (2021), https://doi.org/10.1016/j.cub.2021.04.041

STAR★METHODS

KEY RESOURCES TABLE

REAGENT or RESOURCE	SOURCE	IDENTIFIER
Antibodies		
Rabbit polyclonal anti-PBP2b	Morlot et al.[12]	N/A
Rabbit polyclonal anti-enolase	Morlot et al.[12]	N/A
Bacterial and virus strains		
Streptococcus pneumoniae R800 *rpsL1* ; Str^R	Lefevre et al.[48]	N/A
Streptococcus pneumoniae D39 Δ*cps* Δ*pbp2b* < > *aad9// ΔbgaA::kan-t1t2-*P_{fcsK}*-pbp2b* ; Kan^R $Spec^R$	Tsui et al.[17]	N/A
Chemicals, peptides, and recombinant proteins		
((*R*)-2-amino-3-azidopropanoyl)-D-alanine (aDA-DA)	This paper	N/A
(R)-2-Amino-3-azidopropanoic acid hydrochloride (aDA)	Jena Bioscience	Cat# CLK-AA004-10
Click-iT Alexa Fluor 647 DIBO Alkyne (DIBO-AF647)	Thermofisher	Cat# C20022
Cysteamine (MEA)	Sigma-Aldrich	Cat# 30070
Catalase from bovine liver	Sigma-Aldrich	Cat# C40
Glucose oxidase type VII from *Aspergillus niger*	Sigma-Aldrich	Cat# G2133
Paraformaldehyde (PFA)	Electron Microscopy Sciences	Cat# 15710
Agarose D5	Euromedex	Ref# D5-E
Deposited data		
Raw phase contrast, bright field, diffraction-limited and dSTORM images	This paper	https://zenodo.org/record/4573897#.YII_ZKEpBPY
Raw western blot images	This paper	https://zenodo.org/record/4573897#.YII_ZKEpBPY
3D Spneu cell wall animated model ArtOfIllusion	This paper	https://zenodo.org/record/4573897#.YII_ZKEpBPY
3D Spneu cell wall geometrical model Excel	This paper	https://zenodo.org/record/4573897#.YII_ZKEpBPY
Software and algorithms		
Metamorph	Molecular Devices	https://www.moleculardevices.com/
Volocity	Quorum Technologies	https://quorumtechnologies.com/volocity
ImageJ	Schneider et al.[49]	https://imagej.nih.gov/ij/
FIJI	Schindelin et al.[50]	https://imagej.net/Fiji
ThunderSTORM	Ovesný et al.[51]	https://zitmen.github.io/thunderstorm/
GraphPad Prism Version 8.0	GraphPad	https://www.graphpad.com:443/
Art of Illusion	Peter Eastman	http://www.artofillusion.org/
Other		
Precision cover glasses, No. 1.5H, 24 X 50 mm, 170 ± 5 mm	Marienfeld	Cat# 0107222
Precision cover glasses, No. 1.5H, 22 X 22 mm, 170 ± 5 μm	Marienfeld	Cat# 0107052
TetraSpeck Microspheres	Thermofisher	Cat# T7279

RESOURCE AVAILABILITY

Lead contact

Further information and requests for resources and reagents should be directed to and will be fulfilled by the Lead Contact, Cecile Morlot (cecile.morlot@ibs.fr).

Please cite this article in press as: Trouve et al., Nanoscale dynamics of peptidoglycan assembly during the cell cycle of *Streptococcus pneumoniae*, Current Biology (2021), https://doi.org/10.1016/j.cub.2021.04.041

Materials availability

There are restrictions to the availability of the aDA-DA probe. Due to the time required for chemical synthesis, this material will be available through a collaboration with Yung-Sing Wong (yung-sing.wong@univ-grenoble-alpes.fr).

Data and code availability

The datasets and models generated during this study are available on the Zenodo platform (https://zenodo.org/record/4573897#.YIl_ZKEpBPY).

EXPERIMENTAL MODEL AND SUBJECT DETAILS

Fifty-μL glycerol stocks of non-encapsulated strains of *S. pneumoniae* R800 and D39 *Δcps* (wild-type and *pbp2b* depletion strains),[17,45,48] frozen at OD_{600nm} = 0.3, were used to inoculate 1 mL of CY medium.[52] Cultures were grown at 37°C in a static CO_2 incubator, diluted twice into 10 mL of pre-warmed CY medium ($1/10^{th}$ volume) to reach steady-state growth, and treated subsequently for PG labeling as described in the Method details section.

For the *pbp2b* depletion strain, the same protocol was used to reach steady-state growth except that 2% L-fucose was added to the CY medium. At this stage, the culture was split in two samples, one was further grown in the presence of 2% L-fucose. Depletion of PBP2b was achieved by washing the second sample once and diluting it into 10 mL of CY medium without L-fucose ($1/10^{th}$ volume). Cells were further grown at 37°C until they reach OD_{600nm} = 0.3 before treatment for PG labeling, as described in the Method details section.

METHOD DETAILS

Preparation of PG labeling reagents

All starting materials were obtained from commercial sources and were used without further purification. NMR spectra were performed on a Bruker Advance 400 MHz for ^{1}H-NMR spectra and 100 MHz for ^{13}C-NMR spectra. Chemical shifts are reported in ppm (δ) relative to the solvents: ^{1}H δ(CD_3OD) = 3.3 ppm, ^{13}C δ(CD_3OD) = 49.15 ppm. Accurate mass spectra were recorded on a time-of-flight (TOF) spectrometer (Waters, XEVO G2-S QTof).

The aDA-DA probe (((*R*)-2-amino-3-azidopropanoyl)-D-alanine) was synthesized according to the path shown in Figure S1A. 2-(trimethylsilyl)ethyl (*tert*-butoxycarbonyl)-D-alaninate was obtained according to the Van Nieuwenhze's process.[23] 2-(Trimethylsilyl) ethyl ((*R*)-3-azido-2-((*tert*-butoxycarbonyl)amino)propanoyl)-D-alaninate (80 mg, 0.27 mmol) was diluted in a solution of HCl in dioxane (4 N, 2 mL) and the mixture was stirred for 2 h at room temperature (RT). The solvent was removed under vacuum and allowed to dry under high vacuum (oil pump) for 4 h and the deprotected product was used as such for the next step. This compound was mixed with (*R*)-3-azido-2-((*tert*-butoxycarbonyl)amino)propanoic acid (63.6 mg, 0.37 mmol) and the mixture was dissolved in dry CH_2Cl_2 (5 mL). HATU (1-[Bis(dimethylamino)methylene]-1H-1,2,3-triazolo[4,5-b]pyridinium 3-oxide hexafluorophosphate; 115 mg, 0.30 mmol) and Hünig's base (78.3 mg, 0.61 mmol, diluted in 0.3 mL of CH_2Cl_2) were successively added and the mixture was stirred overnight at RT. The solvent was then removed, and ethyl acetate was added. After it was washed with an aqueous solution of 10% citric acid followed by 5% $NaHCO_3$, the organic layer was dried over $MgSO_4$ and evaporated. After flash chromatography (silica gel, 15% ethyl acetate/cyclohexane), (trimethylsilyl)ethyl ((*R*)-3-azido-2-((*tert*-butoxycarbonyl)amino)propanoyl)-D-alaninate was isolated as a colorless oil (73 mg, 0.18 mmol, 66%) ; ^{1}H NMR (500 MHz, $CDCl_3$) δ (ppm) 0.05 (s, 9H), 1.02 (m, 2H), 1.42 (d, *J* = 7.1 Hz, 3H), 1.47 (s, 9H), 3.54 (dd, *J* = 12.4, 5.5 Hz, 1H), 3.82 (dd, *J* = 12.4, 4.9 Hz, 1H), 4.24 (m, 2H), 4.35 (m, 1H), 4.54 (m, 1H) ; ^{13}C NMR (125 MHz, $CDCl_3$) δ (ppm) – 1.4 (3 × CH_3), 17.4 (CH_2), 18.4 (CH_3), 28.4 (3 × CH_3), 48.6 (CH), 52.4 (CH_2), 53.9 (CH), 64.2 (CH_2), 80.9 (C), 155.5 (C), 169.1 (C), 172.7 (C) ; HRMS (ESI+) m/z calc. for $C_{16}H_{31}O_5N_5SiNa$ $[M+Na]^+$ 424.1987, found 424.1983.

The compound 2-(trimethylsilyl)ethyl ((*R*)-3-azido-2-((*tert*-butoxycarbonyl)amino)propanoyl)-D-alaninate (312 mg, 0.78 mmol) was diluted in TFA (5 mL) in an ice bath and the mixture was stirred for 4 h at RT. The solvent was removed under vacuum and the product was dried under high vacuum (oil pump) for 4 h. Dry ether (10 mL) was added and the mixture was stirred overnight under argon. Following filtration, drying under high vacuum and HPLC purification, aDA-DA was obtained as a solid (150.4 mg, 0.48 mmol, 61%) ; ^{1}H NMR (500 MHz, CD_3OD) δ (ppm) 1.41 (d, *J* = 7.3 Hz, 3H), 3.73 (dd, *J* = 13.4, 7.5 Hz, 1H), 3.92 (dd, *J* = 13.4, 4.0 Hz, 1H), 4.00 (dd, *J* = 7.5, 4.0 Hz, 1H), 4.37 (m, 1H); ^{13}C NMR (125 MHz, CD_3OD) δ (ppm) 18.1 (CH_3), 50.6 (CH), 52.6 (CH_2), 54.0 (CH), 118.2 (q, *J* = 292.0 Hz, CF_3), 163.2 (q, *J* = 35.0 Hz, C), 167.6 (C), 176.6 (C) ; HRMS (ESI+) m/z calc. for $C_6H_{12}O_3N_5$ $[M+H]^+$ 202.0935, found 202.0933.

A 500-mM stock solution of aDA-DA was prepared by resuspending the desiccated powder into 100% DMSO. Aliquots were stored at −80°C. Intermediate 10-mM stock solutions were prepared in commercial DPBS (calcium- and magnesium-free, from ThermoFisher) and stored at −20°C.

The aDA (azido-D-Ala) probe was purchased from Jena Bioscience. The powder was resuspended at 500 mM into 100% DMSO, diluted to 10 mM into DPBS and aliquots were stored at −20°C.

Click-iT Alexa Fluor 647 DIBO alkyne (DIBO-AF647) was purchased from ThermoFisher. The powder was resuspended at 10 mM into 100% DMSO, diluted to 500 μM into DPBS and aliquots were stored at −20°C.

Please cite this article in press as: Trouve et al., Nanoscale dynamics of peptidoglycan assembly during the cell cycle of *Streptococcus pneumoniae*, Current Biology (2021), https://doi.org/10.1016/j.cub.2021.04.041

PG labeling in S. pneumoniae cells

Cultures of *S. pneumoniae* cells in exponential growth phase (OD_{600nm} 0.3) were incubated for 5 min in CY medium (without or with 2% L-fucose) containing 2.5 mM aDA-DA. Cells were then fixed overnight on ice, in the culture medium supplemented with 0.5-X DPBS and 2% (v/v) paraformaldehyde (PFA). For pulse-chase labeling experiments, after the 5-min incubation period in the presence of aDA-DA, cells were pelleted (7,000 × g, 5 min, RT) and resuspended into fresh medium. Incubation at 37°C was continued for 15 min and cells were fixed as described above.

Following PG labeling with aDA-DA, cells were pelleted and resuspended into DPBS containing 35 μM DIBO-AF647. Samples were incubated for 1 h at RT to allow for optimal click reaction, and cells were washed 3 times with 1 mL of DPBS before observation by conventional fluorescence microscopy and preparation of sacculi. For dSTORM imaging, cells were resuspended into a buffer containing 25 mM NaCl, 75 mM Tris-HCl pH 8.0, 10% (w/v) D-glucose, 100 mM cysteamine (β-mercaptoethylamine), 1X GLOX mix [40 $\mu g \times mL^{-1}$ catalase from bovine liver (Sigma-Aldrich), 0.5 $mg \times mL^{-1}$ glucose oxidase type VII from *Aspergillus niger* (Sigma-Aldrich)].

To study PG labeling upon methicillin or D-cycloserine treatment, cultures of *S. pneumoniae* cells in exponential growth phase (OD_{600nm} 0.3) were incubated for 30 min in CY medium containing 0.125 $mg \times mL^{-1}$ D-cycloserine or for 1 h in CY medium containing 0.3 $\mu g \times mL^{-1}$ methicillin. Cells were then incubated with 2.5 mM aDA-DA or 2.5 mM aDA during 5 min, fixed overnight and labeled with DIBO-AF647 as described above.

Sacculi preparation

For preparation of sacculi, exponentially growing cells were incubated simultaneously with 2.5 mM aDA-DA and 35 μM DIBO-AF647 during 5 min. Efficiency of the fluorescent labeling was checked by conventional fluorescence microscopy. Cells were then added dropwise into boiling 8% sodium dodecyl sulfate (SDS) and boiled for 1 h. Sacculi were washed 5 times with 1 mL DPBS prior to incubation with 20 $\mu g \times mL^{-1}$ DNase and 20 $\mu g \times mL^{-1}$ RNase in 100 mM Tris-HCl pH 7.5, 20 mM $MgCl_2$ for 2 h at 37°C on a rotating wheel. After addition of 2 mM $CaCl_2$ and 200 $\mu g \times mL^{-1}$ proteinase K, sacculi were further incubated overnight at 37°C on a rotating wheel. Finally, sacculi were washed 3 times with DPBS before imaging.

Conventional optical microscopy

For phase contrast and conventional fluorescence, samples were observed at RT between a microscope slide and a coverslip, using a motorized two-deck Olympus IX83 optical microscope equipped with a UPFLN 100X O-2PH/1.3 objective and an ORCA-Flash4.0 Digital sCMOS camera from Hamamatsu. Fluorescence of AF647 was excited using a 635-nm LED, a multi band LED-DA/FI/TR/CY5/CY7-A filter set and a bandpass 684/24 emission filter (Semrock). Images were acquired using the Volocity software package. For quantitative comparisons of fluorescence intensity, images were acquired with identical illumination and acquisition parameters.

dSTORM setup and acquisition method

For dSTORM imaging of cells oriented along their longitudinal axis, samples were mounted between a slide (High-precision, No. 1.5H, 24 X 50 mm, 170 ± 5 mm, Marienfeld) and a coverslip (High-precision, No. 1.5H, 22 X 22 mm, 170 ± 5 μm, Marienfeld) previously treated with ozone and eventually sealed with colorless nail polish.

For preparation of agarose pads containing microholes, the silica mold harboring micropilars with diameters ranging from 0.8 to 1.3 μm was produced as described in Söderström et al.[32] The silica mold was placed on top of 2% (w/v) melted agarose until solidification. After removal of the mold, the microhole-agarose pad was equilibrated with dSTORM buffer (without GLOX) for 30 min. The dSTORM buffer was then replaced with the cell sample in dSTORM buffer. After 10 min of incubation at RT, the sample was removed at the surface of the agarose pad, which was washed 3 times with dSTORM buffer to remove cells that would not have entered the microholes. Finally, the agarose pad was covered with an ozone-treated coverslip and sealed with tape.

Images were acquired at 20°C with a home-built PALM/STORM setup based on an Olympus IX81 inverted microscope equipped with diode-pumped solid-state lasers at 405 nm (CrystaLaser) and 643 nm (Toptica Photonics). To achieve wide-field illumination, circularly polarized laser beams were focused to the back focal plane of a × 100 1.49-numerical-aperture (NA) oil immersion apochromatic objective lens (Olympus). The laser illumination intensities were tuned by an acoustico-optical tunable filter (AOTF; Quanta Tech). Fluorescence images were acquired with an Evolve 512 back-illuminated EMCCD camera (Photometrics) controlled by the MetaMorph software (Molecular Devices).

For single molecule localization microscopy, the AF647 dye was exposed to a continuous 643 nm illumination with a constant laser power density of 1.7 $kW \times cm^{-2}$ at the beam center. All dSTORM data were collected over 15,000 frames recorded with an exposure time of 50 ms (20 Hz). The blinking density was maintained all along the data collection by ramping up a 405-nm laser from 0.1% to 3% of a typical maximal value of 50 $W \times cm^{-2}$.

For diffraction-limited images, the sample was illuminated at 643 nm with 0.5% of the maximal laser power (1.7 $kW \times cm^{-2}$).

dSTORM image reconstruction

All data processing was realized with the ThunderSTORM ImageJ/FIJI plugin,[49–51] including determination of the localization precision and quantification of the number of localizations. Potential drift in the focal plane was corrected using 100-nm TetraSpeck Microspheres (ThermoFisher) as fiducial markers. TetraSpeck Microspheres were added to the sample so that about 4 beads were present in each microscopy field. For microhole experiments, the drift was corrected with the cross-correlation tool under

Please cite this article in press as: Trouve et al., Nanoscale dynamics of peptidoglycan assembly during the cell cycle of *Streptococcus pneumoniae*, Current Biology (2021), https://doi.org/10.1016/j.cub.2021.04.041

ThunderSTORM.[51] Image rendering was achieved through normalized Gaussian blurring with a reconstructed pixel size of 12 nm. The spatial resolution of the reconstructed dSTORM images was calculated using the FIRE ImageJ/FIJI plugin.[53]

Measurement of the labeling patterns

To determine the geometrical factors that best describe the pneumococcal shape and growth, measurements of the labeled regions were performed in the following manner with ImageJ.[49] The values of the diameters d, D_1, D_2 and of the labeling width w, W_1 and W_2, as defined in Figure 3A were obtained by plotting the signal intensity along a line positioned over the feature of interest and measuring the distance between the points at half the maximal intensity. The same method was used to measure the total cell length l, as well as the length of external hemispheres L_{H1} and L_{H2} in "butterfly" cells (Figure 3A), using the non-specific cytoplasmic background signal.

For labeling patterns observed radially (in vertical or angled bacteria), the diameters d_{out}, d_{in} and the radial thickness r of the labeled region, as defined in Figure 4D, were measured as above along a line positioned across the longest axis of the imaged ellipses.

Cryo-electron microscopy (cryo-EM)

For cryo-EM, 4 μL of *S. pneumoniae* R800 cells in exponential growth were loaded onto a Quantifoil R3.5/1 holey copper grid (Quantifoil Micro Tools GmbH, Germany). Vitrification of the sample was performed manually (blotting the sample for 1-2 s and plunging rapidly the grid into liquid ethane cooled with liquid nitrogen). The frozen grid was transferred into a 300 kV POLARA electron microscope (FEI). The images were taken under high dose conditions at 300 kV (80 $e^- \times Å^{-2}$), with a magnification of 12,000 and a defocus between 4 and 5 μm using a CCD camera (GATAN ultrascan USC 4000).

Geometrical model of cell growth and labeling

The animated geometrical model was implemented using the free open source 3D animation software Art of Illusion by Peter Eastman. The whole model was produced as an animated 3D-texture within a static rectangular parallelepiped. The mature cell was modeled as a prolate ellipsoid. Taking the longitudinal axis as the x axis, the equator as its origin, and L the length of a mature single cell ($L = 2L_H$), the radius of the cell around this axis (R_{out}) is given by the elliptic curve:

$$R_{out\,(x)} = \sqrt{y_{out}^2 + z_{out}^2} = \sqrt{1 - \left(\frac{x}{L/2}\right)^2}$$

As the new cell length $l^*/2$ grows along x with time, R_{out} at $x = l^*/2$ is the radius of the septal outer edge circle ($R_{out} = d/2$). Taking the length C at which the septum is closed, the radius of the septal inner edge circle (R_{in}) at $x = l^*/2$ is given by:

$$R_{in\,(x)} = \sqrt{y_{in}^2 + z_{in}^2} = \sqrt{1 - \left(\frac{x}{C/2}\right)^2}$$

To account for an acceleration of the growth along the x axis, $l^*/2$ depends on time according to:

$$l^* \Big/ 2_{(t)} = \frac{Lt(1 + At)}{2(1 + A)}$$

where A is an acceleration factor. Note that in this equation, t and A are dimensionless and t is expressed as a fraction of the generation time, which is defined as 1. The $(1+A)$ denominator is a normalization factor that ensures that a division is completed at $t = 1$. We have set $R_{max} = D/2 = 1$, so that in the above equations $L/2$ takes the numerical value of the elliptic factor $E = L/D$.

Determination of the geometrical parameters

To determine the geometrical factors used in the ellipsoid geometrical model (Table S1), measurements performed on pulse-labeled lying cells (Figure 3A) were analyzed as follows.

The largest diameter D was calculated as the average of the measured equatorial diameters D_1 and D_2 (horizontal red line in Figures S5B and S5C). Division has just started at these sites so that the measured diameter should negligibly underestimate the largest diameter D.

To determine the diameter d_G at which the daughter cell generation starts, we plotted as a function of the diameter d the presence (arbitrary value of 1) or absence (arbitrary value of 0) of labeling at equatorial sites. By fitting a sigmoid function to these data, we obtained d_G as the value of the inflexion point (Figure 3E). The same method was used to determine l_G, the length at which the next generation begins, by plotting the presence or absence of equatorial labelings as a function of the length $l^* = l\text{-}L$ (Figure S5D).

To obtain the length L of a fictive mature single cell, we fitted the measurements of the septal diameter d as a function of the cell length l to an elliptic curve (Figures S5B and S5C, black curve):

$$d_{(l)} = D\sqrt{1 - \left(\frac{l - L}{L}\right)^2}$$

Please cite this article in press as: Trouve et al., Nanoscale dynamics of peptidoglycan assembly during the cell cycle of *Streptococcus pneumoniae*, Current Biology (2021), https://doi.org/10.1016/j.cub.2021.04.041

Note that the fit of $d_{(l)}$ was performed for $l\text{-}L \leq l_G$, since the cell length increases faster after the daughter-cell division has started. The good agreement of the value of L determined by fitting the diameter as a function of the cell length with the value of L determined as $2L_H$ (measured directly) indicates that a prolate ellipsoid is a good approximation of the pneumococcal shape.

The labeling pulse is applied for 5 min, but since growth is likely perturbed during this time, we had to determine to what fraction P of a complete cell cycle the pulse length corresponds. We observed that the width of the labeling was greater when it occurred in older cells. In particular, the labeling at the equatorial sites was narrower than at the parental division site. To account for this difference, we introduced in the model the longitudinal acceleration factor A. The length of the new cell $l^* = l\text{-}L$ as a function of time, where the division is completed in $t = 1$, is then given by:

$$l^*_{(t)} = \frac{Lt(1+At)}{(1+A)}$$

The width of labeling after a pulse P ending at time t is:

$$w_{(t)} = l^*_{(t)} - l^*_{(t-P)}$$

The length l^* as a function of the septal diameter d is:

$$l^*_{(d)} = L\sqrt{1-(d/D)^2}$$

Combining the above expressions gives the dependence of the width of labeling on the cell length or septal diameter:

$$w_{(l^*)} = \frac{P\left(\sqrt{L^2+4AL(1+A)l^*} - APL\right)}{1+A}$$

We could extract the pulse length P and the acceleration factor A by fitting the above function to the data of w against l^* (Figures S5E and S5F). Note that we considered only 0.15 μm < l^* < $L\text{-}l_G$, since the above equation for $w_{(l^*)}$ is not valid for $l^* < l^*_{(P)}$, where $w = l^*$, and $l^*_{(t)}$ is not valid when the daughter division has started. In principle, to extract the A and P parameters, we could have used the d data instead of l^* values with the relationship:

$$w_{(d)} = \frac{PL\left(\sqrt{1+4A(1+A)\sqrt{1-(d/D)^2}} - AP\right)}{1+A}$$

However, since d varies little and remains close to D for a large part of the generation time, the great scatter prevented meaningful fitting of the measurements.

To estimate a value for C, the stage at which the septum is closed, we analyzed measurements of the outer and inner diameters (d_{out} and d_{in}) of the labeling rings of cells trapped in microholes (Figures S5G–S5J). If t corresponds to the moment of the measurement at the end of the labeling pulse, labeling at d_{out} occurred at $t\text{-}P$. The length of cells at time t was calculated from d_{out} as:

$$l^*_{(d_{out})} = \frac{L\left(\left(\frac{-1+\sqrt{1+4A\sqrt{1-\left(\frac{d_{out}}{D}\right)^2}(1+A)}}{2A}\right)L\right)+P\left(1+A\left(\left(\frac{-1+\sqrt{1+4A\sqrt{1-\left(\frac{d_{out}}{D}\right)^2}(1+A)}}{2A}\right)L\right)+P\right)}{(1+A)}$$

The values of d_{in} were plotted against l^* (Figures S5G and S5H) to extract C from a fit to the elliptic curve (magenta curve in Figures S5G and S5H):

$$d_{in(l^*)} = D\sqrt{1-\left(\frac{l^*}{C}\right)^2}$$

Alternatively, by combining the two previous equations, we could obtain the expression of d_{in} as a function of d_{out} and fit the resulting curve directly to the d_{in} and d_{out} measurements (Figures S5I and S5J). The latter representation (Figures S5I and S5J) is less intuitive than the representation of the diameters as a function of the length (Figures S5G and S5H) but allows visualization of all the data, whereas the translation of measured outer diameters into length imply the loss of data points with $d_{out} > D$. In both representations, we have included the theoretical position of the diameters d_{out}, d, $d_{in(t\text{-}P)}$ as gray lines. In Figures S5G and S5H, the d_{out} measurements (solid symbols) align with the theoretical curve since these data were used to calculate the l^* values.

Note that we omitted from the fit the data at high values of d_{out} (or small values of l^*) (open blue symbols in Figures S5G–S5J). The geometrical model implies that the inner diameter d_{in} is equal to D at the onset of the division, and that is not what is observed.

Please cite this article in press as: Trouve et al., Nanoscale dynamics of peptidoglycan assembly during the cell cycle of *Streptococcus pneumoniae*, Current Biology (2021), https://doi.org/10.1016/j.cub.2021.04.041

Considering a minimal measurable distance in the dSTORM images of about 30 nm (corresponding to the spatial resolution of our images), d_{in} should plateau in R800 cells at about 0.72 μm in early division, whereas it is observed to plateau at about 0.65 μm. One reason for this discrepancy may be the lack of measurements of the largest diameters at equatorial sites, which are often faintly labeled. It is also possible that the simple model is incorrect regarding very early division stages, which may involve an initial burst of septal synthesis. Since the purpose of this analysis was to parametrize the stage of the septum closure, we forced the fit to $D = 0.8$ μm at $l^* = 0$ μm and considered only data from older cells ($d_{out} < 0.75$ μm, $l^* > 0.45$ μm for R800; $d_{out} < 0.95$ μm, $l^* > 0.5$ μm for $D39_{\Delta cps}$) (magenta in Figures S5G and S5H).

The smaller measurements (in green) were also omitted because after septum closure, the labeling ring only results from peripheral synthesis; in those instances, d_{in} does not correspond to the leading edge of a closing septum but to the outer edge of the septum at the end of the pulse. We therefore ignored data from older cells ($d_{out} < 0.6$ μm, $l^* > 0.8$ μm for R800; $d_{out} < 0.75$ μm, $l^* > 0.9$ μm for $D39_{\Delta cps}$). All cells showing a labeling disk ($d_{in} = 0$) were also omitted from the fit, since they could have completed their septum before the end of the pulse.

Surface area considerations

The variation of the rate of PG synthesis along the cell cycle evidenced by the increase and decrease of the number of dSTORM localization (Figure 3F) prompted us to examine how surface area production occurs according to the geometrical model with two assumptions: the absence of elasticity and the fact that all PG synthesis generates surface area.

With these hypotheses, at the completion of the division, the septal wall has contributed $\pi D^2/4$ units of area while the elongation has added a further $\frac{\pi DL}{4\left(\sqrt{1-\frac{D^2}{L^2}}\right)}\arcsin\left(\sqrt{1-\frac{D^2}{L^2}}\right)$ units of area to each new hemisphere. Consequently, with the length and diameter measured for an average R800 cell, peripheral and septal synthesis would contribute comparable amounts of surface to the daughter cell (about 0.66 μm^2 and 0.50 μm^2, respectively in R800 cells).

To understand how this production of new surface happens during the cell cycle, we calculated the area produced by septation and peripheral elongation by unit of time (the pulse time). While the total surface area of an ellipsoid can be calculated, it is not possible to calculate simply the surface area of a segment of ellipsoid. We therefore approximated the new peripheral surface generated during a pulse time by a cone segment. Since the pulse time is short, this approach underestimates the area by at most 4%. Calculation of the rate of surface area production according to the geometrical model reveals that the rate of peripheral surface generation increases and decreases moderately during the cell cycle while the rate of septal surface generation rises sharply and drops to zero after septum closure (Figure S6A). Consequently, the rate of new area generated by the model correlates well with the numbers of dSTORM localizations used as a proxy for PG synthesis (Figures S6B and S6C). The calculation shows that the rise and decline of surface production is dominated by the rate of septum formation and is little affected by the longitudinal growth acceleration. In contrast, the relation between the rate of septal closure and that of septum splitting has a large influence on the overall rate of surface generation. In our model, points of the outer edge of the septum (i.e., the site of splitting) follow an elliptic path to the new pole, as required to generate an ellipsoid. Points of the inner edge of the septum also, arbitrarily, follow an elliptic curve to the point of septum closure, so that the radial width of the septum increases first slowly and accelerates steadily until septum completion.

Although the rigid model presented above can generate most of the observed labeling patterns, it is likely oversimplified. Several possible complications can be thought of. PG is known to have some elasticity.[46,47] Since the septal wall does not experience turgor pressure and the hemispheric envelope does, it is expected that the cell wall undergoes some expansion following septum cleavage due to turgor pressure. Compared to the rigid model, including elasticity, besides slightly modifying the shape of the growing hemisphere, would somewhat decrease the contribution of peripheral synthesis to cell elongation. A second assumption of the calculations presented above is that peripheral synthesis generates additional surface area. It is also possible that some PG synthesis at the outer edge of the septum adds a new layer of material on the inner face of the cell wall without increasing the surface. In this case, the amount of PG incorporated at the periphery of the septum may be greater than estimated solely by the surface increase. A third assumption implied by the above considerations is a uniform thickness and density of the PG. Finally, our model assumes a constant and rapid activity of the L,D-carboxypeptidase DacB, which trims tetrapeptides into tripeptides following insertion of new PG and can thus remove part of the aDA-DA labeling.[30] If either of these properties were to differ significantly in various regions, the apparent relationship between the estimated surface area and the dSTORM localization counts would be spurious.

QUANTIFICATION AND STATISTICAL ANALYSIS

Figures were prepared and statistics were performed using GraphPad Prism version 8.00 for PC (GraphPad Software, https://www.graphpad.com:443/). The statistical details describing the quantification and measurements of localization patterns (including the definition of center, dispersion and precision of measures, the statistical tests used, the exact value of the n number of analyzed cells) can be found in the Results section and in the figure legends.

Current Biology, Volume *31*

Supplemental Information

Nanoscale dynamics of peptidoglycan assembly during the cell cycle of *Streptococcus pneumoniae*

Jennyfer Trouve, André Zapun, Christopher Arthaud, Claire Durmort, Anne Marie Di Guilmi, Bill Söderström, Anais Pelletier, Christophe Grangeasse, Dominique Bourgeois, Yung-Sing Wong, and Cecile Morlot

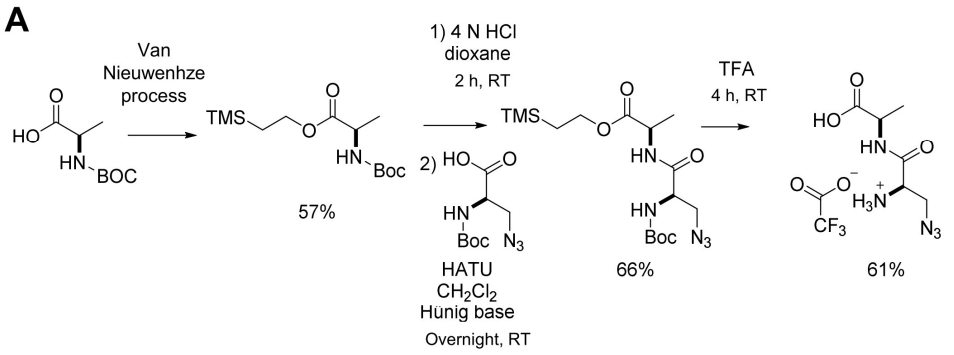
A
Van
Nieuwenhze
process
TMS
HO
HN
BOC
Boc
57%
1) 4 N HCl
dioxane
2 h, RT
2) HO
HATU
CH_2Cl_2
Hünig base
Overnight, RT
66%
TFA
4 h, RT
CF_3
H_3N
N_3
61%

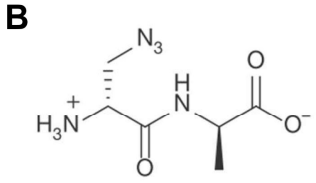
B
N_3
H_3N
O
H
N
O^-

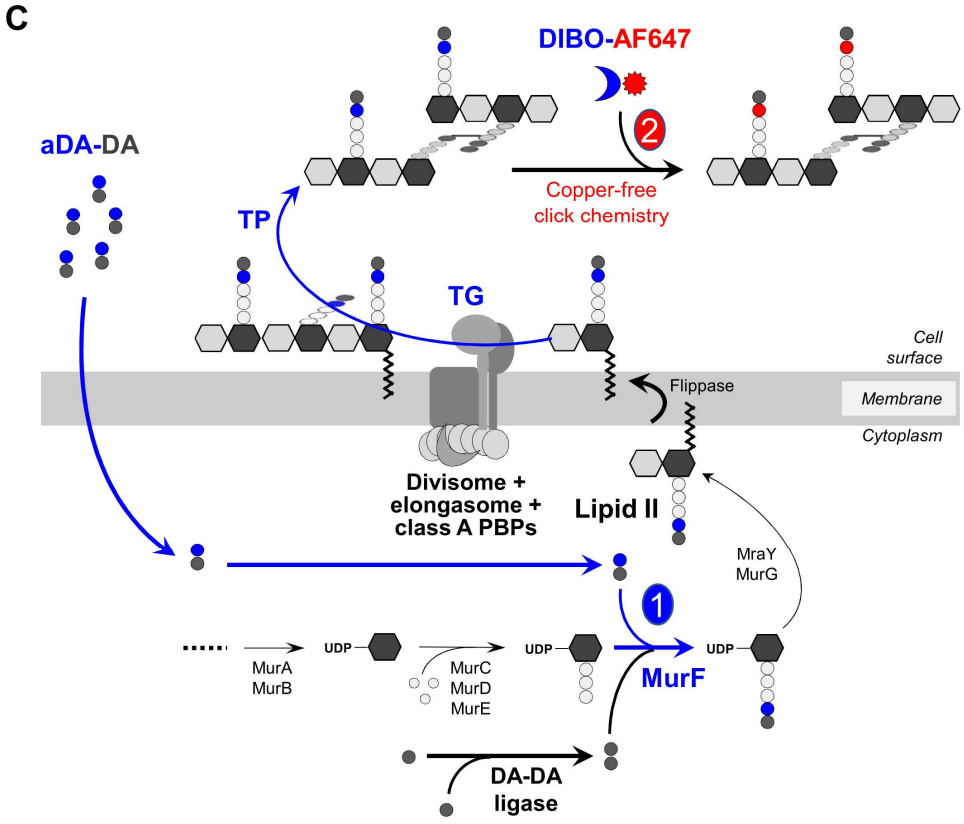
C
DIBO-AF647
aDA-DA
TP
2
Copper-free
click chemistry
TG
Cell
surface
Membrane
Cytoplasm
Flippase
Divisome +
elongasome +
class A PBPs
Lipid II
MraY
MurG
1
UDP
MurA
MurB
MurC
MurD
MurE
MurF
DA-DA
ligase

Figure S1. Schematic representation of the experimental strategy. Related to Figure 1.

A. Chemical synthesis path of the aDA-DA probe (((*R*)-2-amino-3-azidopropanoyl)-D-alanine). 2-(trimethylsilyl)ethyl (*tert*-butoxycarbonyl)-D-alaninate was obtained according to the Van Nieuwenhze's process[S1]. 2-(trimethylsilyl)ethyl ((*R*)-3-azido-2-((*tert*-butoxycarbonyl)amino)propanoyl)-D-alaninate was diluted in a solution of HCl in dioxane and the mixture was stirred for 2 h at room temperature (RT). The product was mixed with (*R*)-3-azido-2-((*tert*-butoxycarbonyl)amino)propanoic acid and the mixture was dissolved in dry CH_2Cl_2. HATU (1-[Bis(dimethylamino)methylene]-1H-1,2,3-triazolo[4,5-b]pyridinium 3-oxide hexafluorophosphate) and Hünig's base were successively added and the mixture was stirred overnight at RT. The solvent was then removed, and ethyl acetate was added. The product trimethylsilyl)ethyl ((*R*)-3-azido-2-((*tert*-butoxycarbonyl)amino)propanoyl)-D-alaninate was diluted in TFA and stirred for 4 h at RT to obtain the aDA-DA compound. **B.** Chemical structure of the aDA-DA probe. **C.** Schematics of the predicted incorporation of the aDA-DA probe into the PG precursor by MurF (1). The azido-labeled lipid II is polymerized by SEDS and PBPs from the elongasome and the divisome, as well as class A PBPS, and the labeled glycan chains are cross-linked by PBPs into the existing PG. The azido-labeled new peptide chains are eventually conjugated to the AF647 dye through a copper-free click-chemistry reaction between the azide and DIBO groups (2).

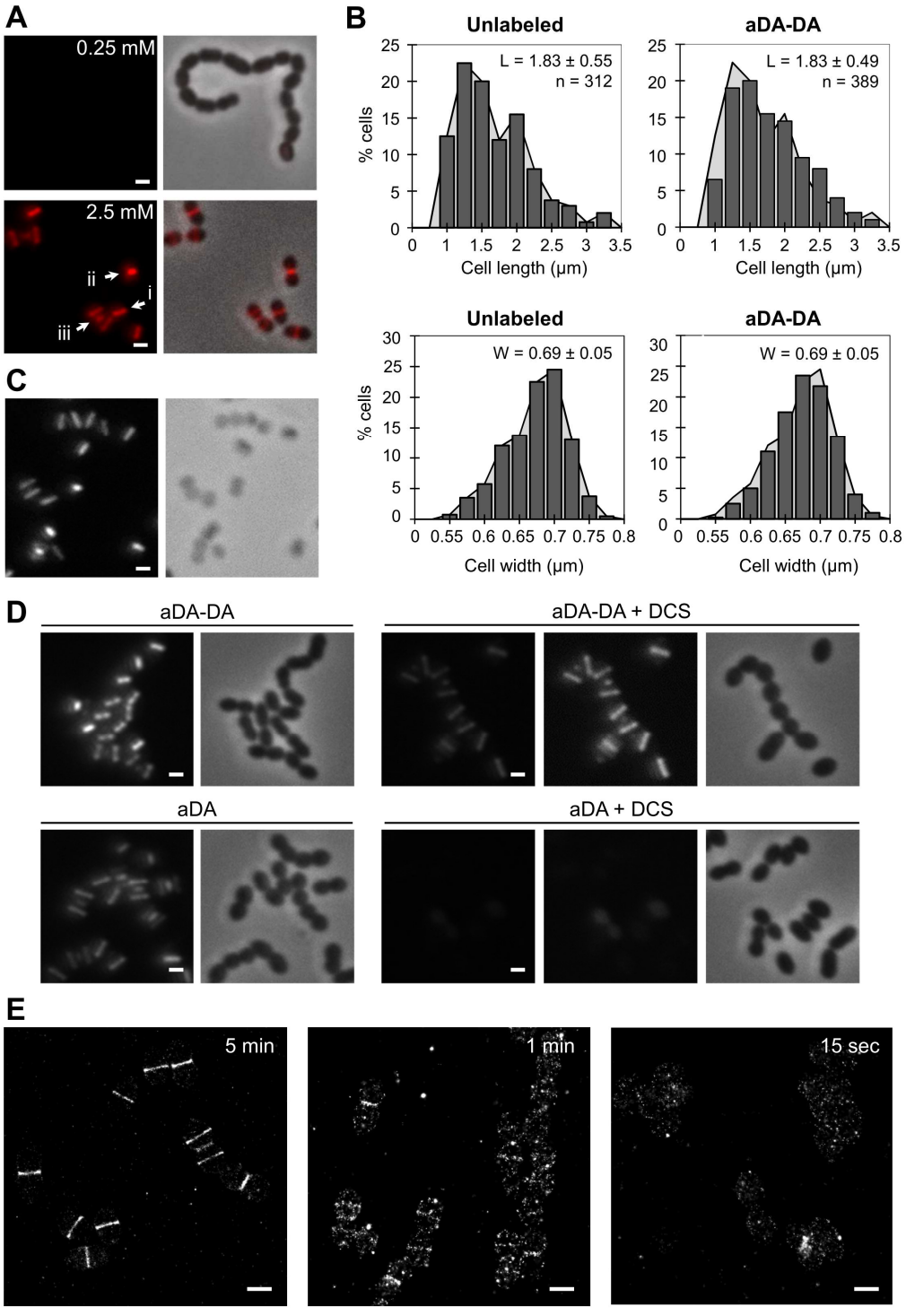
A
0.25 mM
2.5 mM
ii
i
iii
B
Unlabeled
aDA-DA
L = 1.83 ± 0.55
n = 312
L = 1.83 ± 0.49
n = 389
% cells
Cell length (µm)
W = 0.69 ± 0.05
Cell width (µm)
C
D
aDA-DA
aDA-DA + DCS
aDA
aDA + DCS
E
5 min
1 min
15 sec

Figure S2. Labeling of pneumococcal PG with D-Ala derivatives. Related to Figure 1. A. Conventional fluorescence microscopy images obtained with 0.25 mM (top panels) or 2.5 mM (lower panels) aDA-DA. Wild-type *S. pneumoniae* R800 cells in exponential growth phase were grown for 5 min in the presence of aDA-DA, fixed, and incubated with 35 µM DIBO-AF647 for labeling before microscopy observation. Left panels show the AF647 signal, right panels show merged phase contrast and AF647 images. All images were recorded with the same acquisition parameters, and signal levels were treated identically for each panel. The probe concentration usually used for HADA and TADA labeling in *S. pneumoniae* (0.25 µM) is not sufficient for aDA-DA labeling. Arrows point at cells in one of the three stages described in figure 2. **B.** Distributions of cell lengths and widths measured in phase contrast images of unlabeled (light grey areas) or cells labeled with aDA-DA (dark grey bars). Mean values, standard deviations and the number cells that were analyzed are given on the graphs. **C.** Sacculi prepared from cells labeled with aDA-DA. The conventional fluorescence microscopy image obtained from the AF647 signal (left panel), as well as the phase contrast image (right panel) are shown. **D.** Labeling of R800 cells with aDA-DA or aDA in the absence or in the presence of 0.125 mg·mL^{-1} D-cycloserine (DCS). AF647 signal and phase contrast images are shown. For experiments performed in the presence of DCS, the contrast of the AF647 signal in the middle image was increased similarly for the aDA-DA and aDA panels. **E.** Reconstructed dSTORM images obtained with *S. pneumoniae* R800 cells incubated with aDA-DA during 5 min, 1 min or 15 sec before being fixed and labeled with DIBO-AF647. Scale bars throughout, 1 µm.

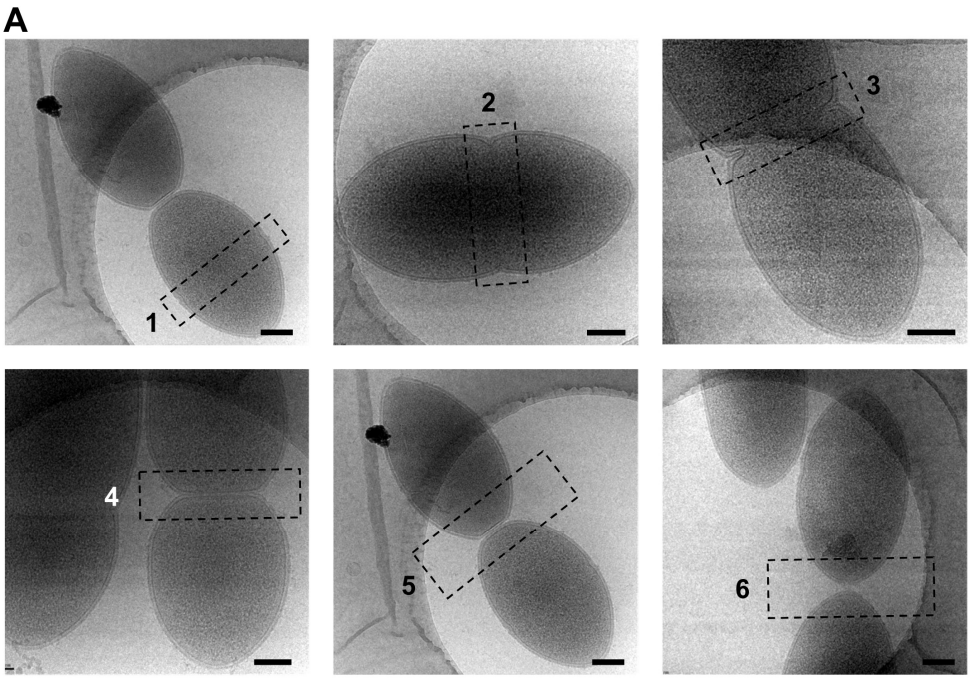
A
1
2
3
4
5
6

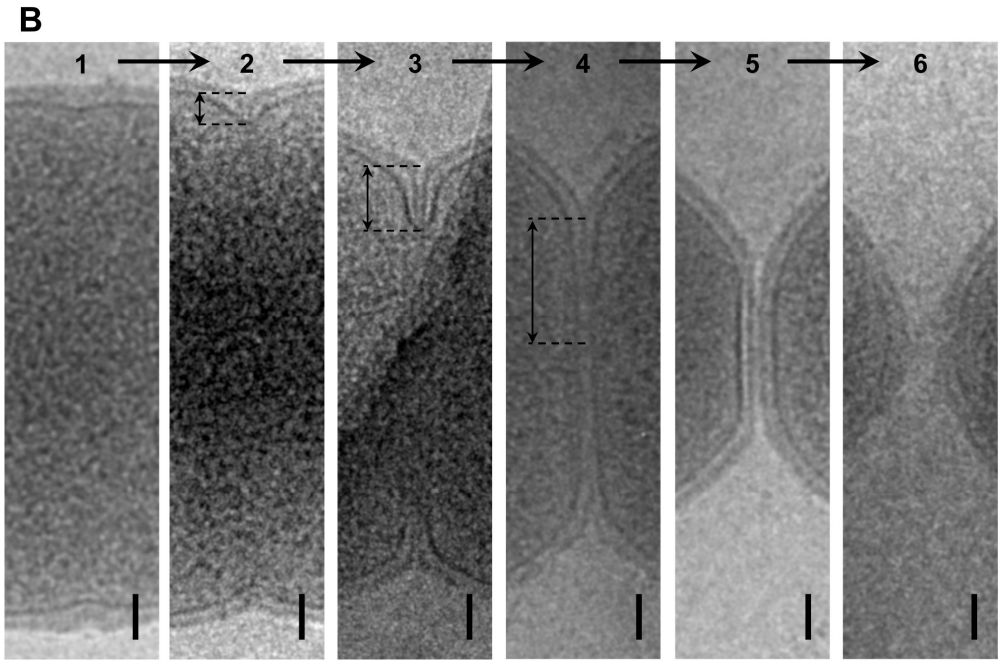
B
1
2
3
4
5
6

Figure S3. Transmission electron microscopy images of whole cells of *S. pneumoniae* R800 at different stages of the cell cycle. Related to Figure 4. A. Exponentially growing *S. pneumoniae* R800 cells were flash frozen in liquid ethane and imaged using a Polara electron microscope. Scale bars, 200 nm. **B.** Zooms of septal regions at successive division steps. Numbers correspond to the dashed-box numbers in panel A. The black double arrows indicate the inner and outer edges of the septum, which define the radial width of the septum. Scale bars, 100 nm.

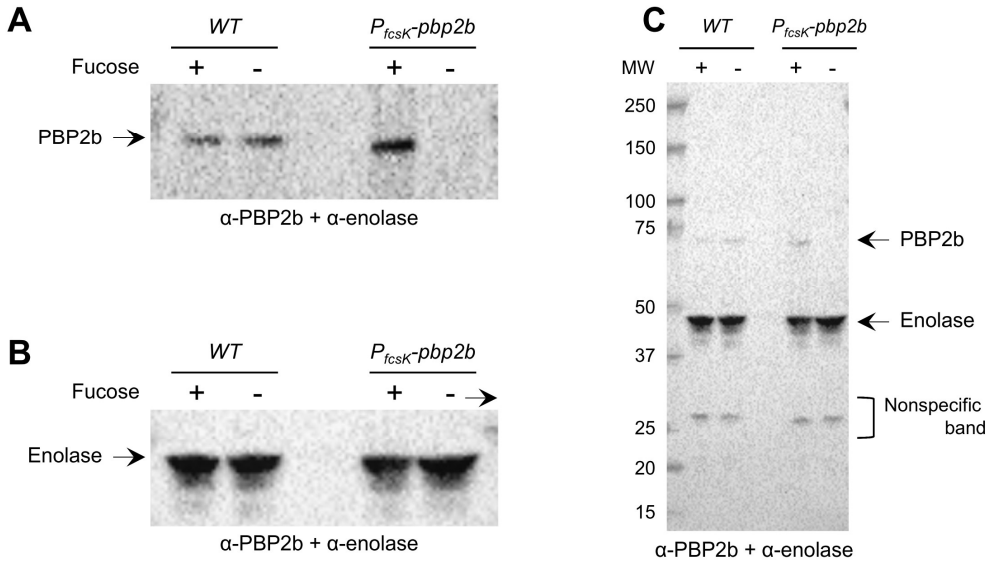

Figure S4. Depletion of PBP2b in *S. pneumoniae* D39 Δ*cps* cells. Related to Figure 4. Immunoblot analysis of whole-cell lysates from *S. pneumoniae* strains D39 Δ*cps* (*WT*), IU7397 (D39 Δ*cps Δpbp2b bgaA::*P_{fcsK}*-pbp2b*) (P_{fcsK}*-pbp2b*) grown in the absence (-) or in the presence (+) of 2% fucose. The depletion of PBP2b was monitored with anti-PBP2b serum and enolase levels were monitored with anti-enolase serum to control for loading. **A.** 120-sec exposure of the anti-PBP2b/anti-enolase western blot aiming at highlighting the band corresponding to PBP2b. **B.** 20-sec exposure of the anti-PBP2b/anti-enolase western blot aiming at highlighting the band corresponding to enolase. **C.** Full view of the anti-PBP2b/anti-enolase western blot shown in panels A and B, with the position of the molecular weight (MW, in kDa) markers.

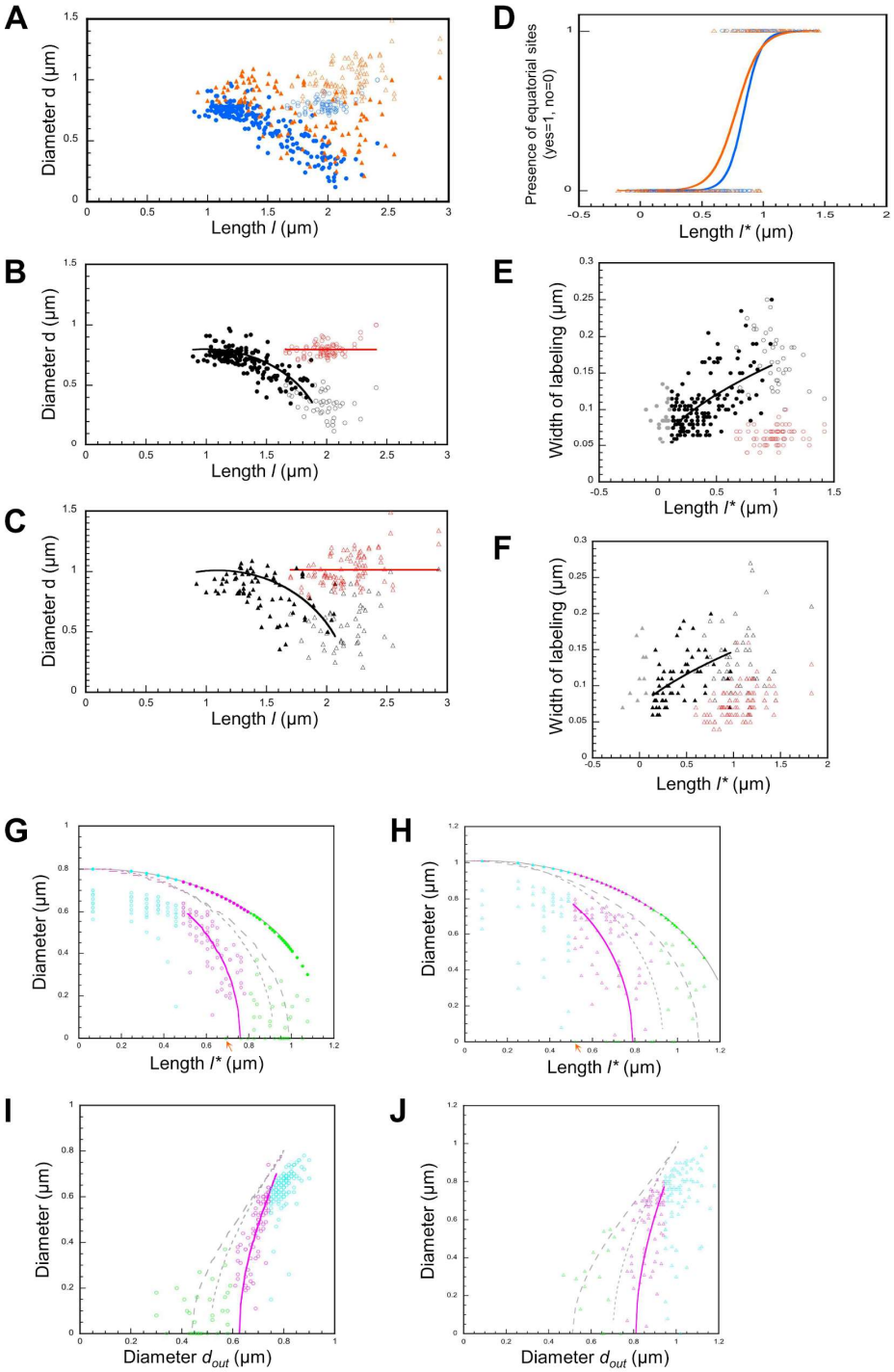
A
Diameter d (µm)
Length l (µm)
B
Diameter d (µm)
Length l (µm)
C
Diameter d (µm)
Length l (µm)
D
Presence of equatorial sites (yes=1, no=0)
Length l* (µm)
E
Width of labeling (µm)
Length l* (µm)
F
Width of labeling (µm)
Length l* (µm)
G
Diameter (µm)
Length l* (µm)
H
Diameter (µm)
Length l* (µm)
I
Diameter (µm)
Diameter d_{out} (µm)
J
Diameter (µm)
Diameter d_{out} (µm)

Figure S5. Determination of the parameters of the geometrical model. Related to the STAR Methods. A. Diameters of parental (*d*, plain symbols) and equatorial (D_1 and D_2, empty symbols) against the cell length *l* measured on R800 (blue) or D39$_{\Delta cps}$ (orange) cells. **B-C.** Fitting of an elliptic curve (black line) to the parental diameter *d* (solid black symbols) plotted as a function of the cell length *l* for R800 (**B**) or D39$_{\Delta cps}$ (**C**) cells. Parental diameters collected on "butterfly" patterns (empty black symbols), i.e. on cells in which the daughter division has started, were not considered for the fit. The largest diameter *D* was determined as the average of equatorial (D_1 and D_2, in red) measurements (red line). **D.** Determination of the length l_G at which the next generation starts in R800 (blue) and D39$_{\Delta cps}$ (orange) cells. The l_G parameter is determined as the inflexion point of a sigmoid fitted to the presence (value = 1) or absence (value = 0) of equatorial labelings against the cell length *l*. **E-F.** Determination of the longitudinal acceleration factor *A* and the pulse time *P* by fitting the longitudinal width *w* of labeling as a function of the cell length l^* for R800 (**E**) or D39$_{\Delta cps}$ (**F**) cells. The graphs show longitudinal widths of the parental (*w*, in black) and equatorial (W_1 and W_2, in red) sites. The black line shows the fit of the function $w_{(l^*)}$ to the data (solid symbols), excluding parental longitudinal widths collected on "butterfly" cells (empty symbols) and on cells younger than the pulse time (l^* < 0.15 µm, grey symbols), as described in the STAR Methods. **G-J.** Determination of the cell length *C* at which the septum closes. The outer and inner diameters d_{out} and d_{in} (solid and open symbol) were measured in microhole-trapped cells. The d_{out} values were transformed in length l^* with the equation $l^*_{(dout)}$ defined in the STAR Methods. The length *C* was determined by fitting an elliptic curve to the measurements of d_{in} versus the length l^* (magenta curve) for R800 (**G**) and D39$_{\Delta cps}$ (**H**) cells. Data at high (cyan) and low (green) d_{out} were omitted from the fit for reasons discussed in the STAR Methods. The grey curves represent the model d_{out}, *d* and $d_{in(t\text{-}P)}$ in solid, long and short dashes, respectively. The distance between the *d* and $d_{in(t\text{-}P)}$ curves represents the separation between the two concentric labeling rings observed in Figure 4. The orange arrows point at cells displaying a full disk with no separation between the two PG synthesis regions, such as the *c2* cells in Figure 4. **I-J.** The same diameter data and curves as in **G-H** but represented versus the diameter d_{out} for R800 (**I**) and D39$_{\Delta cps}$ (**J**) cells.

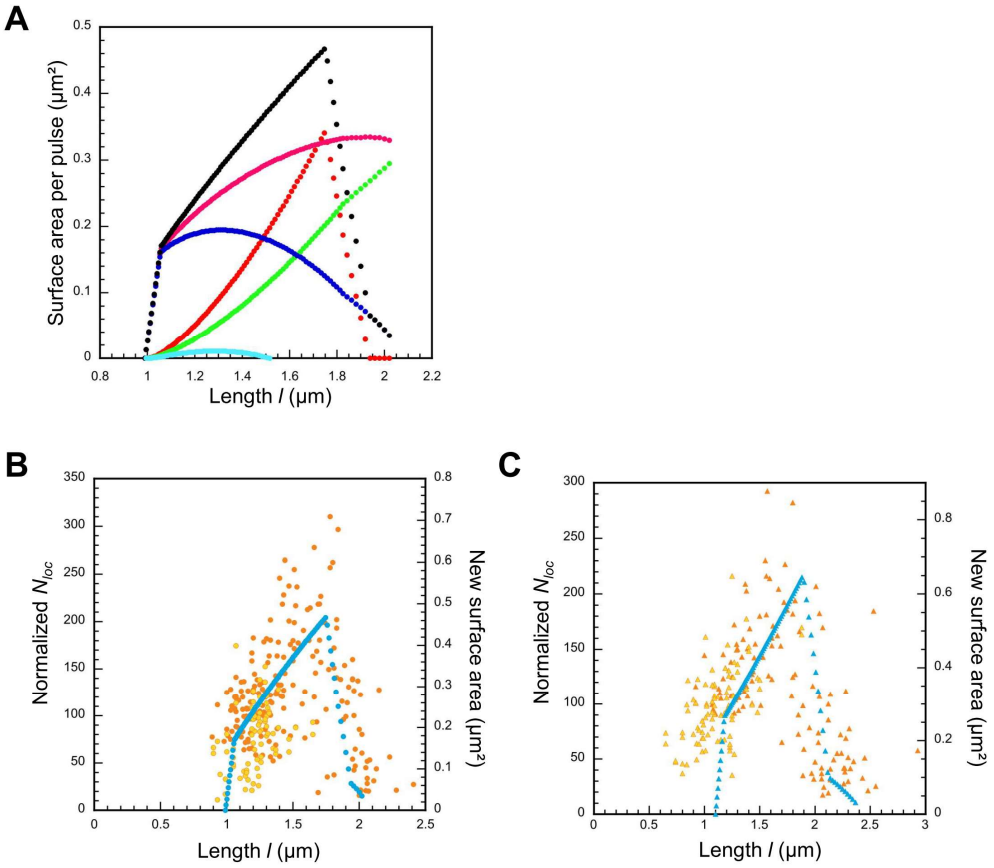

Figure S6. Comparison of the rate of PG synthesis and surface expansion. Related to the STAR Methods. A. Surface expansions during the labeling pulse for one hundred R800 cells with one 100th of generation time age-differences, as calculated with the geometrical model plotted against the length *l* at the end of the pulse. Total surface area (black), septal surface area (red), lateral surface area (magenta), septal to peripheral converted surface area (green), peripheral surface area (blue), and doubly labeled surface area (cyan) generated during the pulse period. **B-C.** Number of dSTORM localizations (orange, dark for parental and light for equatorial sites) from data collected on *S. pneumoniae* R800 (**B**) or D39$_{\Delta cps}$ (**C**), as well as new surface areas (blue) calculated with the geometrical model plotted against the cell length *l*.

	R800	**D39$_{\Delta cps}$**
***D* (µm) (± SE)**	0.80 ± 0.01	1.01 ± 0.01
***L* (µm) (± SE)**	0.99 ± 0.01	1.10 ± 0.02
***E = L/D* (± SE)**	1.24 ± 0.03	1.09 ± 0.03
l_G (µm) (± SE)	0.84 ± 0.01 0.90 (as a fraction of the generation time)	0.78 ± 0.02 0.77 (as a fraction of the generation time)
***A* (± SE)**	0.9 ± 0.2	0.5 ± 0.2
***P* (± SE)**	0.115 ± 0.003	0.106 ± 0.04
***C* (µm) (± SE)**	0.76 ± 0.01 0.84 (as a fraction of the generation time)	0.79 ± 0.01 0.78 (as a fraction of the generation time)

Table S1. Geometrical parameters. Related to the STAR Methods. *D*, maximal cell diameter; *L*, maximal cell length; *E*, elliptic ratio; l_G, cell length at which the next generation starts; *A*, longitudinal acceleration factor; *P*, duration of the labeling pulse; *C*, cell length at which the septum closes; SE, standard error.

SUPPLEMENTAL REFERENCE

S1. Liechti, G.W., Kuru, E., Hall, E., Kalinda, A., Brun, Y.V., VanNieuwenhze, M., and Maurelli, A.T. (2014). A new metabolic cell-wall labelling method reveals peptidoglycan in *Chlamydia trachomatis* . Nature *506*, 507–510.